Fall 12-2015

Rear-Flank Outflow Dynamics and Thermodynamics in the 10 June 2010 Last Chance, Colorado Supercell

Curtis J. Riganti
University of Nebraska-Lincoln, curtis.riganti@gmail.com

Rear-Flank Outflow Dynamics and Thermodynamics in the 10 June 2010 Last Chance, Colorado Supercell

by

Curtis J. Riganti

A THESIS

Presented to the Faculty of

The Graduate College at the University of Nebraska

In Partial Fulfillment of Requirements

For the Degree of Master of Science

Major: Earth and Atmospheric Sciences

Under the Supervision of Professor Adam L. Houston

Lincoln, Nebraska

November, 2015

Rear-Flank Outflow Dynamics and Thermodynamics in the 10 June 2010 Last Chance, Colorado Supercell

Curtis J. Riganti, M.S.

University of Nebraska, 2015

Adviser: Adam L. Houston

On 10 June 2010, the second Verification of the Origins of Tornadoes Experiment (VORTEX2) armada observed the non-tornadic phase of a supercell thunderstorm near Last Chance, Colorado. Tempest unmanned aircraft system (UAS) data collected in the rear-flank outflow revealed what appeared to be an elevated outflow head, turbulent wake, and a cold secondary outflow surge. Surface thermodynamic and kinematic data collected by StickNets and mobile mesonets suggested that the outflow wake may have extended to or very near the surface, perhaps cutting off the leading edge of the outflow at times. Single-Doppler data collected by the NOAA X-Pol Mobile Polarimetric Doppler Radar (NOXP) were supportive of the possibility of a downdraft in the outflow wake being driven by low-level divergence. A conceptual model of the hypothesized rear-flank outflow structure in the non-tornadic phase of the Last Chance supercell is presented. A comparison of the secondary cold outflow surge to previously observed rear-flank internal surges is also presented.

Acknowledgements

I would like to thank my advisor, Dr. Adam Houston, and other committee members, Drs. Matthew Van Den Broeke, and Clinton Rowe for unwavering support, helpful discussion, and direction throughout the course of this project. I would like to thank the University of Nebraska-Lincoln Department of Earth and Atmospheric Sciences for a teaching assistantship and the National Science Foundation for grants AGS-1542760 and IIA-1539070 which made this work possible. Thanks also go to the University of Colorado-Boulder, Texas Tech University, Penn State University, the University of Oklahoma, and other institutions and people who were involved in the VORTEX2 field campaign. I would like to thank Dr. George Limpert, who provided many hours of helpful discussion and technical support throughout the course of this project, as well as the other members (past and present) of the UNL Severe Storms Research Group who provided support and guidance. Outside of the UNL Severe Storms Research Group, I would like to thank Alicia Klees for helpful discussion, and Gordon Carrie and Charles Kuster for technical support. Finally, I would like to thank my family and friends for their constant support and encouragement as this work was completed.

Table of Contents

List of Figures

List of Tables

Chapter 1

Introduction

1.1 Background

For many years, meteorologists have hypothesized that the rear-flank downdraft (RFD) is critical to the formation of tornadoes (the reader is referred to the review of Markowski 2002 and references therein). Under the assumption that there is pre-existing vertical vorticity very close to ground level, convergence/stretching associated with the RFD could amplify this vorticity into a tornado-strength vortex. For vertical vorticity to develop near the ground, a supercell must transport vorticity associated with the storm's mesocyclone to the surface, create vorticity through baroclinicity, or some combination of these two processes. In theory, the RFD can also assist low level vertical vorticity generation due to the horizontal buoyancy gradients which exist within it (and antecedent baroclinic generation of vorticity). The RFD may also transport air rich in angular momentum from aloft to low levels of the storm, where convergence may act to form a low-level maximum in vertical vorticity (Markowski 2002; Davies-Jones 2008).

Via analyses of Doppler radar and *in situ* surface observations collected during the Verification of the Origins of Rotation in Tornadoes Experiment (VORTEX), it was hypothesized that RFDs characterized by higher thermal buoyancy were more likely to support tornadogenesis, due to a higher potential for air in the RFD to accelerate upward

and increase vertical vorticity via stretching (Markowski et al. 2002; Markowski 2002; Grzych et al. 2007; Hirth et al. 2008; Lee et al. 2012). However, it is also likely that the RFD realigns and distributes vorticity that is generated baroclinically within the RFD (Davies-Jones and Brooks 1993), suggesting that tornadogenesis may also be less likely to occur in the absence of a horizontal buoyancy gradient (i.e., having outflow that is too warm for baroclinic vorticity generation). From the observation of vortex lines which arch over hook echoes, it has been inferred that some low-level vertical vorticity in supercells is created baroclinically (Straka et al. 2007). From this observation, it follows that a deficit in the thermal buoyancy of RFDs would be a favorable condition for the formation of low-level vertical vorticity. Therefore, there may exist a range of thermal buoyancy within RFDs (relative to the surrounding air mass) which is most supportive of tornadogenesis and tornado maintenance (Markowski 2008).

Recent *in situ* observations (e.g., Marquis et al. 2000; Mashiko et al. 2009, Lee et al. 2012; Kosiba et al. 2013; Skinner et al. 2014) have identified momentum surges behind the primary rear-flank gust front (RFGF), hereafter referred to as rear-flank internal surges (RFIS), as being instrumental in providing surface convergence needed for stretching of vertical vorticity, and subsequent tornadogenesis. The potential importance of RFIS formation with regard to tornadogenesis underscores the importance of diagnosing the kinematic and thermodynamic processes which lead to their occurrence.

On 10 June 2010, during the second Verification of the Origins of Rotation in Tornadoes Experiment (VORTEX2; Wurman et al. 2012), the NOAA X-Pol (NOXP) Doppler radar, SMART-R 2 (SR2) Doppler radar (Bigggerstaff et al. 2005), StickNet

(Weiss et al. 2008), mobile mesonet surface observing platforms, and the Tempest unmanned aircraft system (UAS; Elston et al. 2011) observed a RFGF, rear-flank outflow (RFO), and rear-flank internal surge of a supercell thunderstorm during its post-tornadic stage. This data set is unique in large measure because surface observations of these features were accompanied by UAS observations. This juxtaposition provided a unique opportunity to study the vertical thermodynamic structure of a rear-flank outflow.

1.2 Overview of the Last Chance Case

Two supercell thunderstorms formed in an upslope flow regime in northeastern Colorado late in the afternoon on 10 June 2010. One supercell initiated at about 22:30 UTC and eventually underwent a merger and weakened (Klees et al. 2014). A second supercell, hereafter referred to as the "Last Chance supercell" due to its proximity to Last Chance, Colorado, also initiated at around 22:30 UTC and produced two tornadoes between about 01:08-01:27 UTC (Klees et al. 2014). After this tornadic phase, the RFGF propagated well ahead of the mid-level mesocyclone and tornado production abated. Structure and evolution of the RFO during this non-tornadic phase, particularly from 01:28-02:10 UTC, is the focus of this study. The reader is referred to the work of Klees et al. (2014) for analysis and discussion of the interaction between the northern and Last Chance supercells and an in-depth analysis of mesocyclone evolution during the non-tornadic phase of the Last Chance supercell.

During its non-tornadic phase, the Last Chance supercell was embedded in an environment characterized by moderate mixed-layer convective available potential energy (MLCAPE), steep mid-level lapse rates above the capping inversion (near dry

adiabatic), and moderate low-level shear (0-3 km storm relative helicity values ranged from 110-152 m^2s^{-2}). Figure 1.1 shows the location of the three soundings launched from 01:37 to 01:40 UTC used to represent the environment relative to the supercells at 01:37 UTC. The soundings were plotted and indices calculated using the SHARPPy package (Halbert et al. 2015).

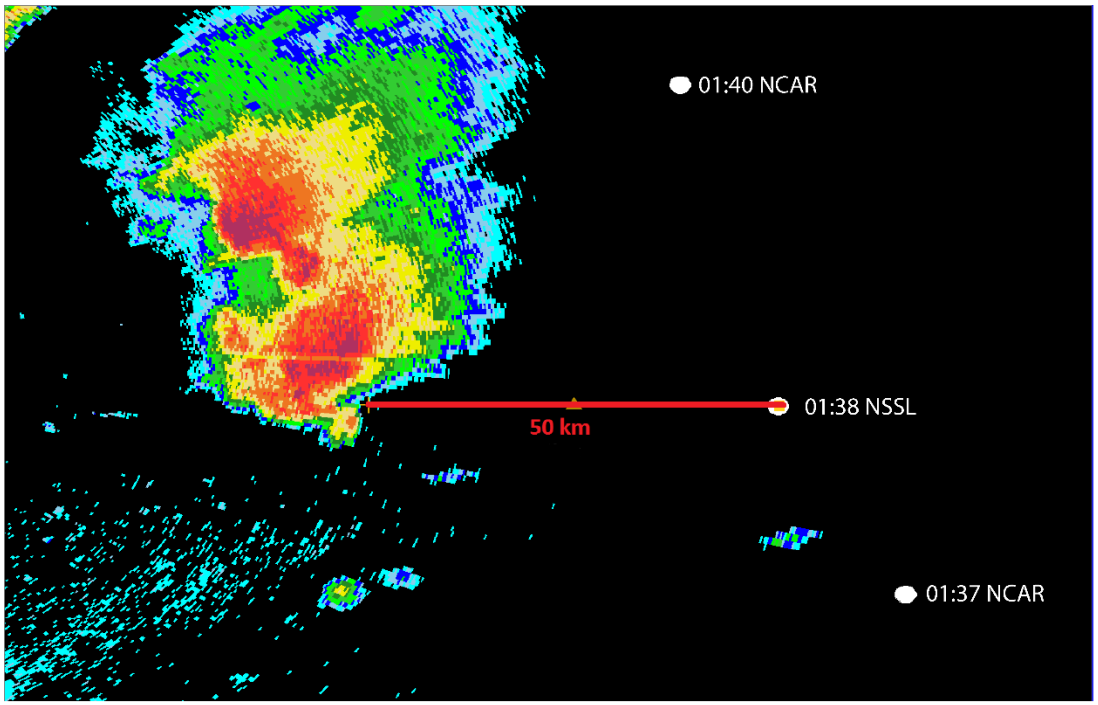

Fig. 1.1: Radar reflectivity factor from KFTG (Denver, CO WSR-88D) with locations of three soundings overlaid (valid near 01:37 UTC).

A thermal inversion was present near the 750 hPa level (Figs. 1.2 and 1.4). This inversion also existed in the 01:37 UTC sounding (Fig. 1.3), though it was located closer to 800 hPa and was accompanied by a sharp inversion near the ground (perhaps due to anvil shadowing effects).

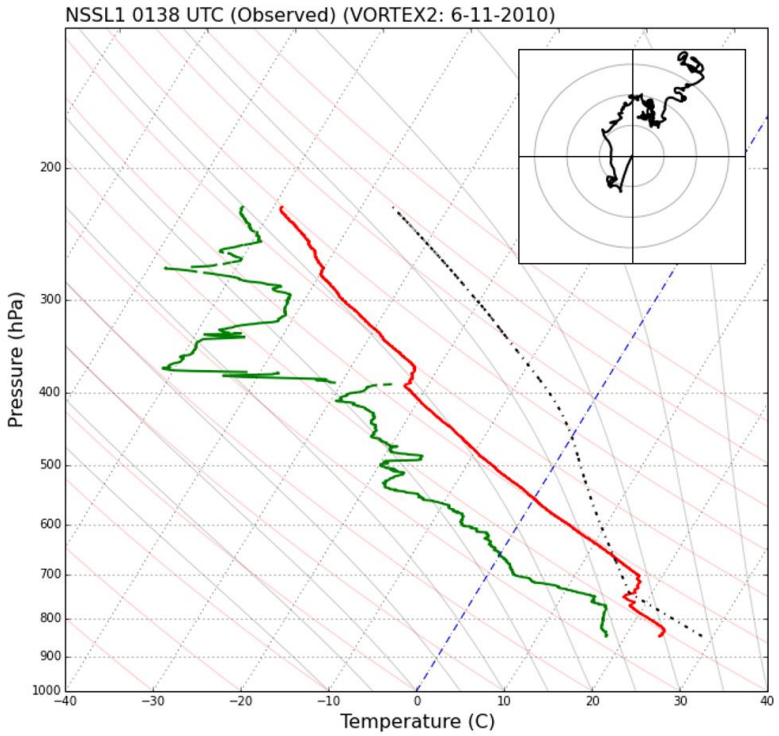

Fig. 1.2: 01:38 UTC NSSL sounding. Hodograph rings are at 10 ms^{-1} intervals. 100 hPa mixed layer parcel trace.

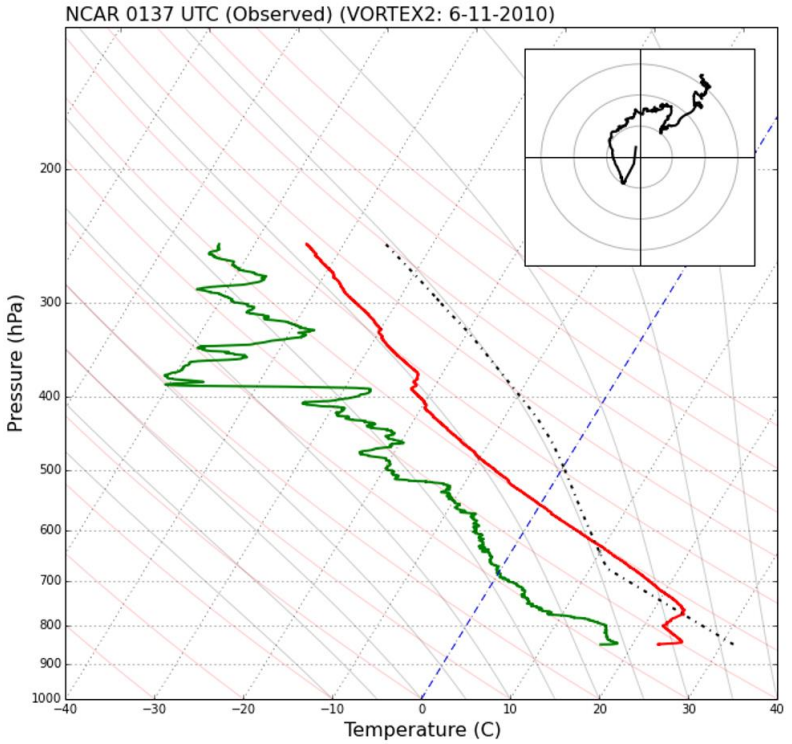

Fig. 1.3: 01:37 UTC NCAR sounding. Hodograph rings every 10 ms^{-1}. 100 hPa mixed layer parcel trace.

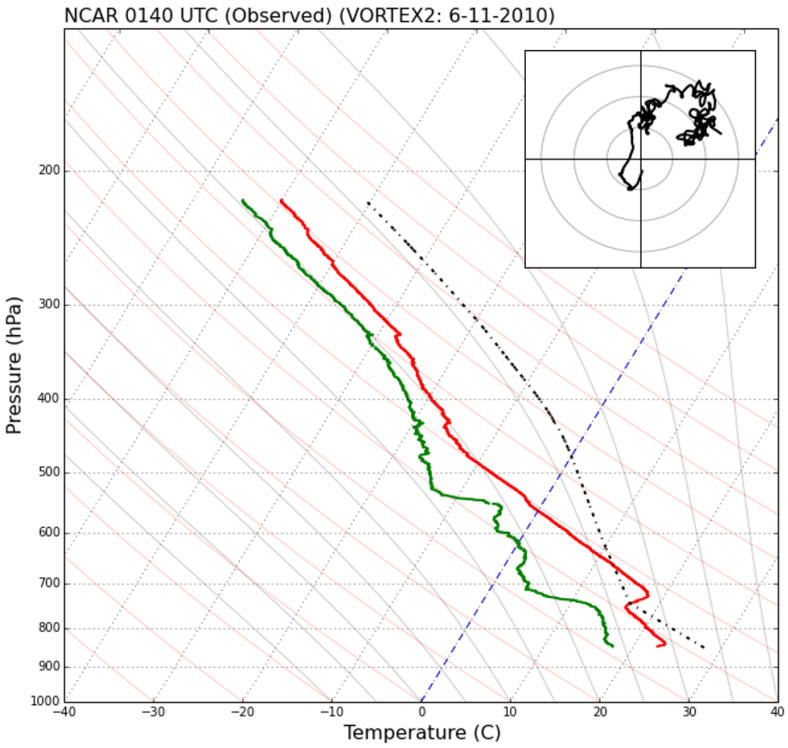

100 hPa MLCAPE: 2879 J/kg
100 hPa MLCIN: -111 J/kg
0-3 km SRH: 110 m2/s2

Fig. 1.4**:** 01:40 UTC NCAR sounding. 100 hPa mixed layer parcel trace; 10 ms^{-1} hodograph rings.

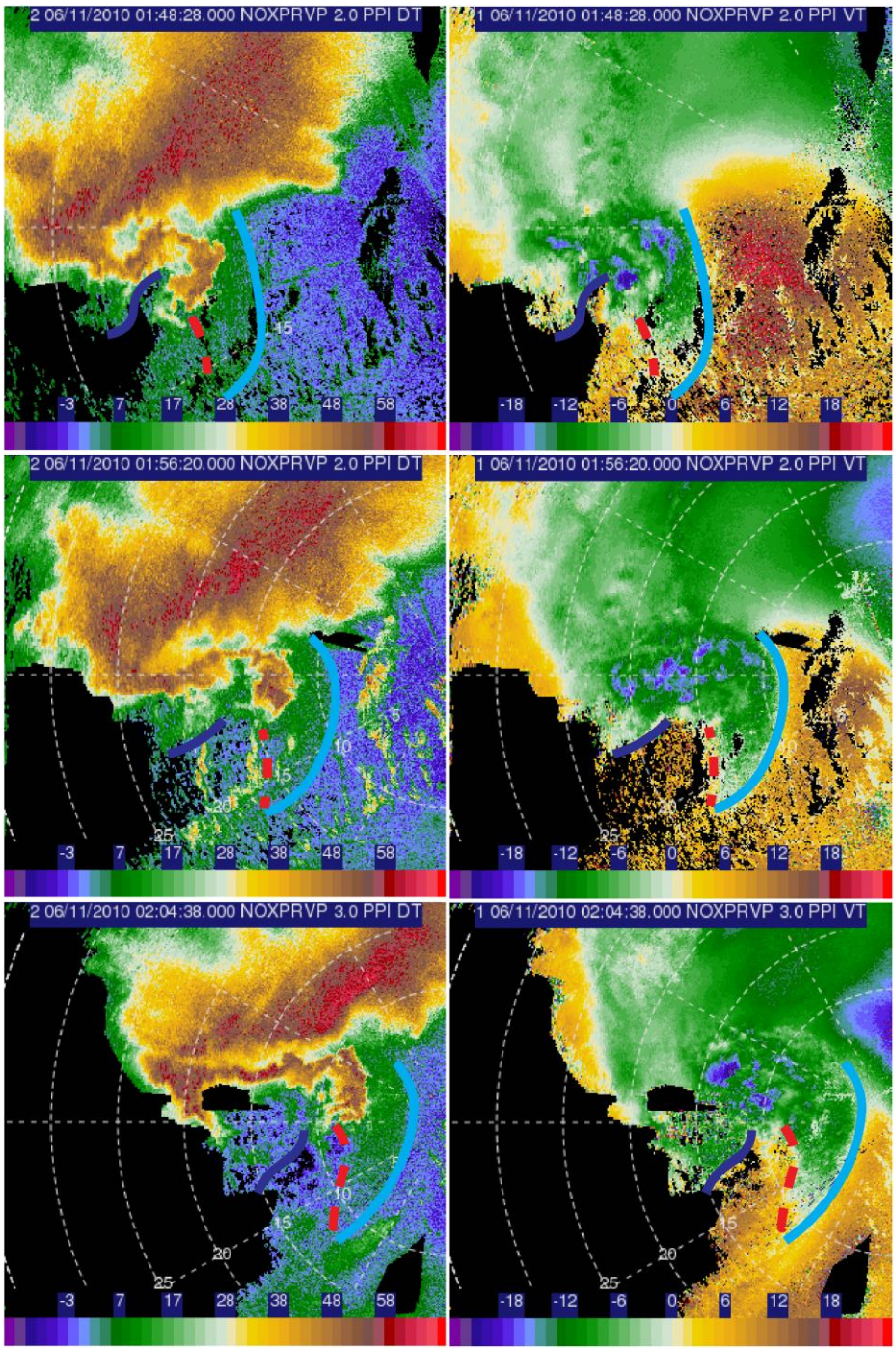

Fig. 1.5: NOXP uncorrected reflectivity (dBZ) (left panels) and radial velocity (ms^{-1}) (right panels). Annotations are: RFGF=solid sky blue line, RFIS=solid dark blue line, leading edge of outflow wake=dashed red line. 8 minute intervals are shown, starting at 01:48 UTC and ending at 02:04 UTC. All except 02:04 UTC are 2.0^0 elevation PPIs; the 02:04 UTC scan was taken at 3^0 elevation.

Between 01:48 UTC and 02:04 UTC, the RFGF (denoted as the solid sky blue line in Fig. 1.5) propagated to the east towards NOXP. As the (RFO) expanded to the

east, a region of outbound radial velocity became clearly visible to the rear of the RFGF, followed by a second area of inbound radial velocity farther to the west (Fig. 1.5). The secondary area of inbound radial velocity is referred to as the RFIS (denoted as the solid dark blue line); this is the RFIS that the UAS, scout mesonet, and StickNets sampled. Meanwhile, the hook echo propagated eastward as well, and took on a flared-out shape (Bluestein et al. 2014).

Chapter 2

Methodology

2.1 Radar Methodology

NOXP, an X-band dual-polarimetric Doppler radar, collected shallow volume scans with seven elevation tilts ranging from 1^0 to 7^0 (Table 1.1). NOXP data were manually quality controlled using Solo3 to align ground clutter with nearby surface clutter targets, subsequently remove ground clutter, remove multiple trip echoes, and de-alias radial velocity. Additionally, radial offsets which existed in some higher tilts in NOXP data were manually corrected by aligning storm scale features (such as the hook echo) to positions in adjacent elevation angles.

Table 1.1: NOXP radar specifications

NOXP Specifications	
Band	X
Half-power beamwidth	0.88°
# of sweeps per volume	7 (1°-7°)
Nyquist velocity	19.93 ms^{-1}
Nyquist Range	59.95 km

2.2 Coordinate System Methodology

Previous studies have examined the thermodynamic characteristics of RFOs in supercells by placing surface observations (both from moving and stationary platforms) in a storm-relative reference frame (e.g., Markowski et al. 2002; Lee et al. 2004; Finley et al. 2008; Lee et al. 2012; Klees et al. 2014). While thermodynamic and kinematic analysis of the Last Chance supercell could also have been performed in a storm-relative framework (as was described in Klees et al. 2014), since the focus of this work is on the rear-flank air masses and attendant boundaries, in-situ data were placed in a *boundary-relative* reference frame. Moreover, the RFGF did not maintain a constant mid-level mesocyclone-relative position. Therefore, placing data in coordinates with respect to the mid-level mesocyclone could not be assumed to produce an analysis which retains information about RFGF-relative positions.

The initial steps taken to place data collected by the Tempest UAS, StickNets, and mobile mesonets into boundary-relative coordinates involved subjectively analyzing the position of the RFGF with observations collected by the KFTG Denver Weather Surveillance Radar-88 Doppler (WSR-88D), SR2, and NOXP. The reader is referred to Table 1.2 for a list of boundary position analysis times and other specifications. Sets of

latitude/longitude coordinates were recorded for each RFGF position by drawing boundaries in the Integrated Data Viewer based on the positions of reflectivity fine lines and inbound/outbound radial velocities at 0.8^0-3.0^0 tilts. As boundaries were drawn farther south of the storm, the positions of the southern ends of the boundaries became more approximate due to weaker signal returns. While this was done to include some of the southernmost StickNet observing stations in the analysis, the boundary-relative positions at the southern edge of the domain should be considered more approximate than those farther north.

Table 1.2: Boundary-relative coordinate system methodology.

Analysis Times (UTC)	Radars Used
1:28:32	KFTG
1:32:50	KFTG
1:37:28	KFTG
1:42:05	NOXP & SR2
1:44:19	NOXP & SR2
1:46:24	NOXP & SR2
1:48:28	NOXP & SR2
1:54:28	NOXP & SR2
1:56:20	NOXP & SR2
1:58:25	NOXP & SR2
2:00:29	NOXP & SR2
2:02:21	NOXP
2:04:25	NOXP
2:06:30	NOXP
2:10:26	NOXP
Latitude Grid Spacing	0.0001°

Once boundary positions at fixed analysis times were collected, intermediate RFGF positions were calculated to create a set of RFGF positions spanning the analysis time frame. First, the pre-determined boundary positions were linearly interpolated to splines on a $1/10000^{th}$ degree spaced latitude grid, such that along each respective latitude

parallel, there existed a set of longitude values that defined east-west positions of the RFGF at different times. Between the fixed analysis times, intermediate longitude values were computed along latitude parallels via linear extrapolation at a 1 Hz frequency, which resulted in a set of latitude/longitude coordinates approximating the RFGF position for every second during the analysis period. Thus, the interpolation along separate latitude parallels accounted for differential boundary motion in the west-to-east direction.

The positions of instruments relative to the RFGF were then calculated. Data from each instrument were linearly interpolated to a 1 Hz frequency. Each instrument's (stationary and moving) distance from the RFGF was calculated using the haversine function, where for every second that data existed, the minimum distance to any point along the RFGF was calculated. If the observation was collected west of the gust front, the distance was recorded as a negative number, while observations east of the gust front were recorded as positive numbers. Data that were collected north or south of the predefined latitude grid were excluded from analysis.

2.3 StickNet Methods

StickNet pods (Weiss et al. 2008) recorded pressure, temperature, relative humidity and wind speed and direction. All StickNets recorded these data at either 10 Hz, 5 Hz, or 1 Hz. Data not recorded at 1 Hz were subsampled for boundary-relative coordinate system processing to a 1 Hz frequency. StickNet data used for this analysis are from a 12-unit south-north array deployed along Colorado Highway 71. Automated quality controls were also applied to StickNet data in order to remove bad or questionable thermodynamic data and wind data (Weiss et al. 2008). Pressure data from the

southernmost probe were subjectively determined to be too high as well, so thermodynamic variables from this probe were excluded from the analysis. Before being plotted on a RFGF-relative plot, wind data were converted to their u and v components and then smoothed with a 20 second Gaussian filter.

2.4 Tempest UAS Methods

The Tempest UAS (Fig. 2.1) collected pressure, temperature, and relative humidity data. The Vaisala RS92 core sensor collected temperature and relative humidity data with response times of 0.5 s and 0.4 s, respectively. An Aeroprobe Corporation Five-Hole Pitch+Yaw sensor also collected 3-dimensional wind data, though these were considered to not be research grade. Altitude data were also recorded from GPS altitude measurements.

Fig. 2.1: Tempest UAS during AVIATE.

Chapter 3

Results

The Tempest UAS collected pressure, temperature, and relative humidity data in the environment to the southeast of the Last Chance supercell and in the supercell's RFO. Data were collected from 01:28 UTC to 02:04 UTC, mainly on a north-south trajectory along Colorado Highway 71 as the primary RFGF and a RFIS translated from west to east across Colorado Highway 71 (Fig. 3.1) to the south of the flared-out hook echo. As discussed previously, the UAS sampled three distinct features within the RFO. First, the primary RFGF can be seen as a gradual decrease in equivalent potential temperature (θ_e) at approximately 01:41 UTC (Fig. 3.2). Equivalent potential temperature then gradually decreased for the following five minutes, which would be expected as the UAS penetrated deeper into the RFO. An increase in θ_e followed from 01:47 to 01:53 UTC. Equivalent potential temperature values during this period reached or exceeded those seen prior to the passage of the RFGF. A rapid decrease in θ_e occurred from about 01:53 to 02:00 UTC, signifying the presence of a cold RFIS (Fig. 3.2). An increase in

equivalent potential temperature to values near those in the air mass immediately in front of the secondary outflow surge then occurred as the UAS travelled southward.

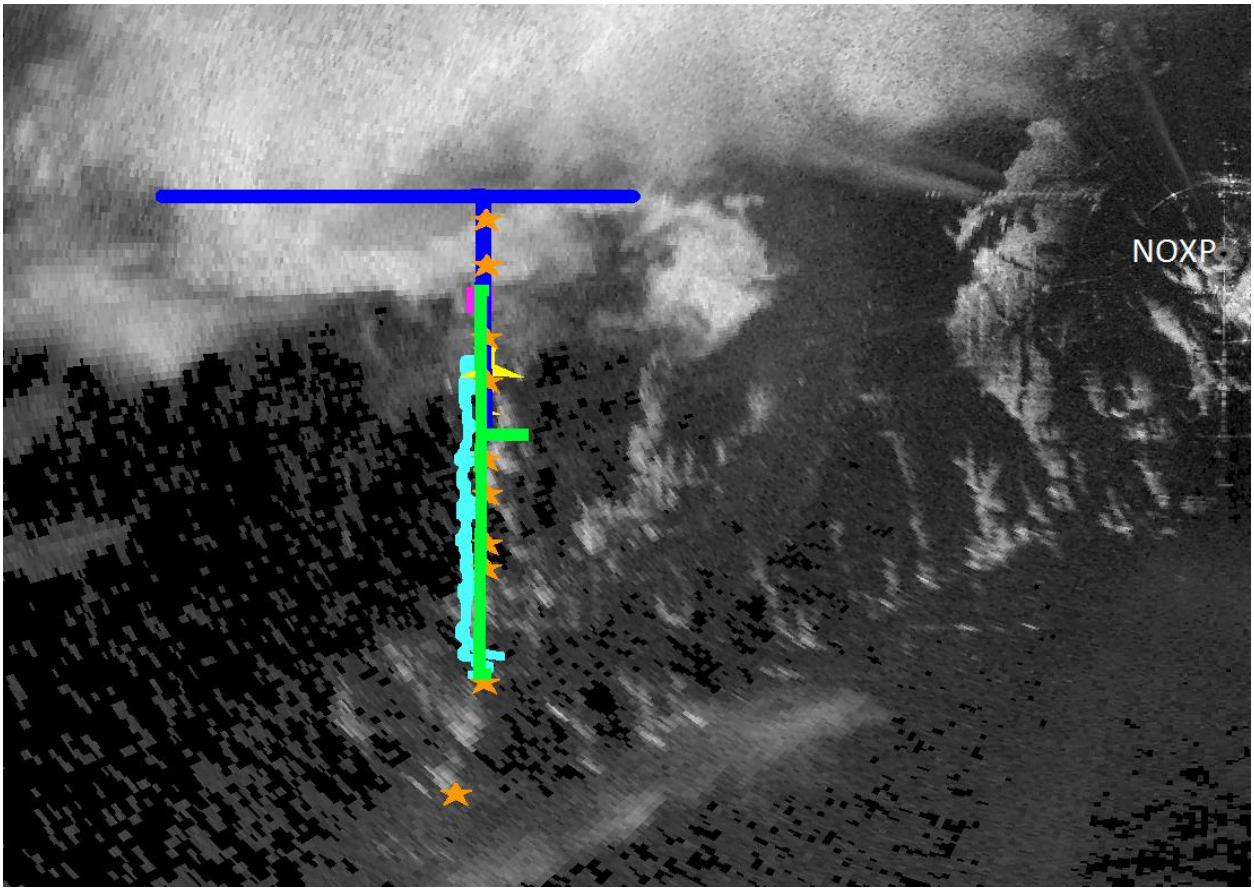

Fig. 3.1: Locations of instruments. Radar image is NOXP 2.0^0 tilt at 01:56:20 UTC, solid blue line represents positions of PSU mobile mesonets from 01:50 UTC to 02:00 UTC, solid green line represents all scout mesonet positions, sky blue line represents all UAS positions, magenta square represents location of scout mesonet at 01:56:20 UTC, yellow airplane represents position of UAS at 01:56:20 UTC, and orange stars represent StickNet locations. As denoted, NOXP is near the right-center edge of the figure.

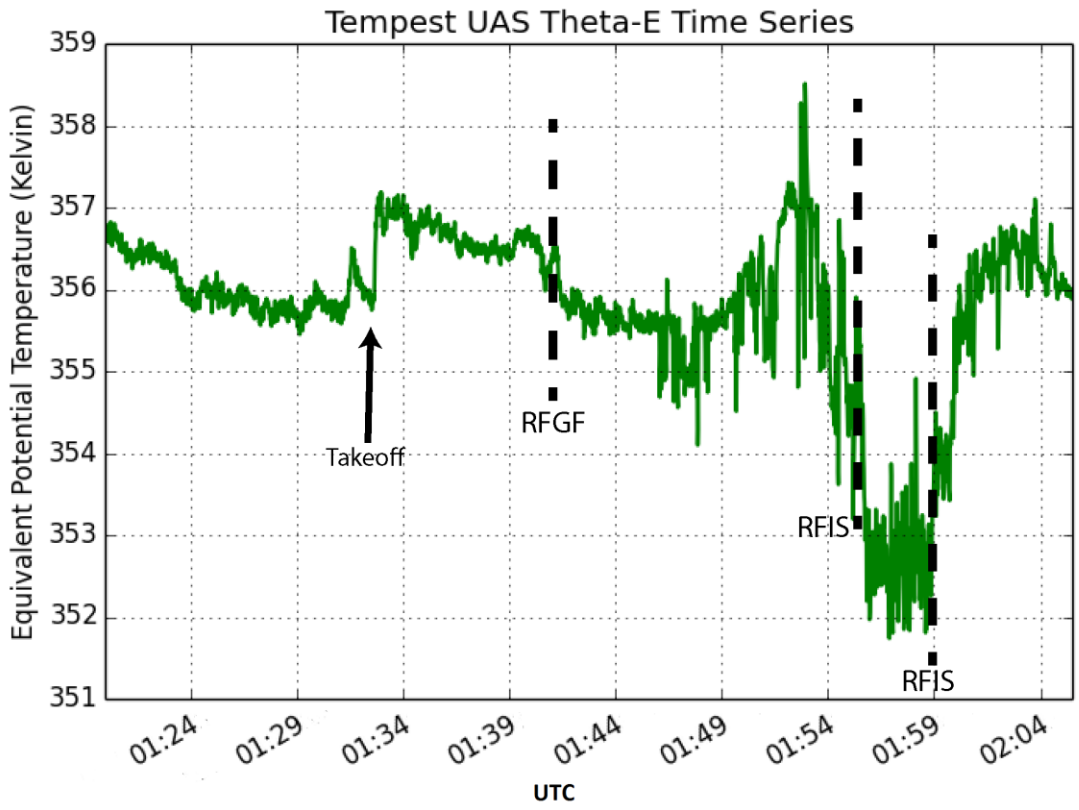

Fig. 3.2: Time series of Tempest UAS equivalent potential temperature (K).

Just before encountering the RFIS (around 01:55 UTC), the UAS altitude rapidly increased by 30-40 m (Fig. 3.3). Since the aircraft autopilot was tasked to stay on an isobaric level corresponding to an AGL height of ~375 m, this quick increase in altitude can be attributed to strong, small-scale ascent and/or a sudden increase in pressure. An increase in pressure was not observed, thus the sudden increase in altitude is most likely a consequence of an updraft, which would be expected at the leading edge of an advancing cold RFIS. A smaller altitude increase occurred as the UAS exited the outflow surge at about 02:00 UTC (about 5-6 minutes after the initial altitude increase), supporting the presence of an updraft tied to a persistent feature within the larger-scale outflow.

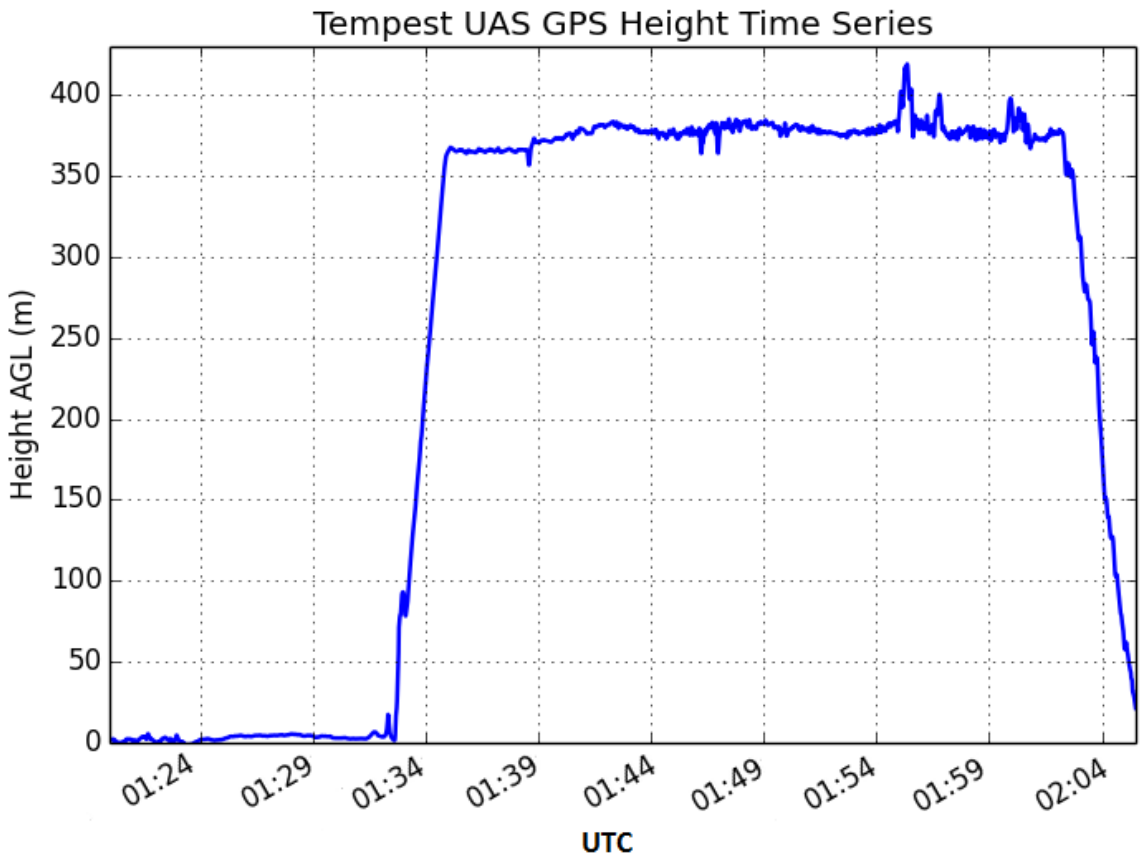

Fig. 3.3: Tempest UAS GPS height (m AGL).

Equivalent potential temperature derived from UAS observations suggest that a distinct air mass similar to the inflow air mass existed within the RFO. In the following analysis, the characteristics of this air mass aloft and at the surface will be examined in a RFGF-relative reference frame. To the west of the RFGF, the primary RFO manifests as a ~1 K decrease in potential temperature (Fig. 3.4a). At about 4.5 km rearward of the RFGF, potential temperature gradually increased back to values consistent with pre-RFGF air (Fig. 3.4a). The air mass to the west of 5 km was generally characterized by higher potential temperature, though several local maxima existed, one at about 6.5 km rearward of the RFGF, and two 8-9 km rearward of the RFGF. The first maximum in potential temperature was roughly co-located with the θ_e maximum within the wake (Fig.

3.4a,b). However, the second and third potential temperature maxima were located in a region where θ_e was relatively low (much closer to primary RFO values than to θ_e values within the wake). The RFIS was then manifest as a rapid decrease in potential temperature to values below those found in the initial RFO. Immediately to the west of the RFGF, in the primary RFO, θ_e decreased by 1-1.5 K. Equivalent potential temperature values then became more variable (though generally increased) from 4.5 km to 5.5 km rearward of the RFGF (Fig. 3.4b). After this period of higher variability, θ_e increased by 2-3 K from 5.5 to 7 km rearward of the RFGF as the UAS progressed northward through the RFO (Fig. 10b). The θ_e values in this region met or exceeded θ_e values in the inflow environment to the east of the RFGF. Between 7 and 8 km rearward of the RFGF, θ_e again became more variable, and, aside from a few points in the range of θ_e in the wake, θ_e decreased back to values characteristic of the initial RFO. The region 8-11 km rearward of the RFGF was characterized by θ_e about 3 K lower than the initial RFO, signifying the presence of the cold RFIS. As the UAS progressed southward, it again encountered θ_e values more characteristic of the inflow air mass.

The same features in the RFO can be seen in other UAS-measured variables, with a few key differences. Water vapor mixing ratio data show a RFO that, in general, was slightly drier than the inflow air mass (Fig. 3.4c). In the localized regions of high potential temperature in the wake, water vapor mixing ratios reached local minima. The second peak in potential temperature (at about 8.5 km rearward of the RFGF) was also characterized by low water vapor mixing ratios (values at or below 13.4 gkg^{-1}), indicating that the warm air within the wake was also, in some areas, very dry. Low water vapor

mixing ratio values were also present in the RFIS, compared both to the inflow environment and the initial outflow (Fig. 3.4c).

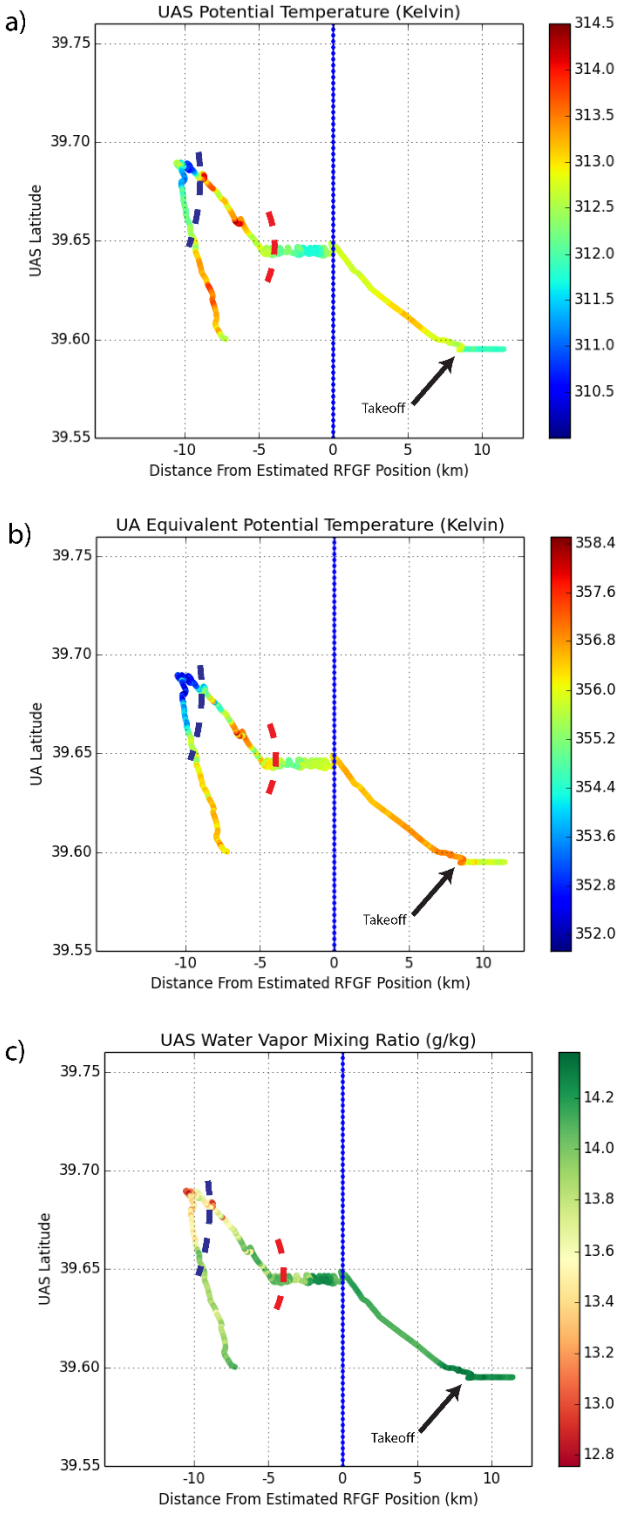

Fig. 3.4: Tempest UAS a) potential temperature, b) equivalent potential temperature, and c) water vapor mixing ratio in latitude vs distance spatial coordinates. The blue line represents the RFGF position, while UAS observations start in the bottom right and continue to the west.

The UAS also revealed the vertical thermodynamic structure of the lowest 350-400 m of the boundary layer inflow region through which the RFGF would have passed. Between ground level and ~380 m AGL, potential temperature increased from roughly 311.8 K to 312.7 K, yielding an approximate vertical potential temperature gradient of 2.37 K km^{-1}. This stable layer was likely present due to anvil shadowing which prevented the formation of an adiabatic or super-adiabatic surface layer. Therefore, the thermal structure of the pre-RFGF boundary layer should have provided some thermodynamic resistance to vertical parcel accelerations.

UAS thermodynamic data exhibited a spatial pattern consistent with an RFO that, above the surface, had been partitioned into an initial outflow head, a turbulent and much warmer wake region, and a RFIS. The initial outflow, in terms of both potential temperature and θ_e, was cold with respect to the inflow environment, but warmer than the RFIS (Fig. 3.4). The large variability of potential temperature in the wake, in contrast to lower variability in the initial RFO, suggests the existence of a turbulent wake, which would be expected behind the head of a density current where Kelvin-Helmholtz instability (KHI) would likely be released (Droegemeier and Wilhelmson 1987; Simpson 1997). Additionally, the higher potential temperature values in the wake, combined with low water vapor mixing ratio, suggests that air within the wake came from outside the RFO.

UAS potential temperature and water vapor mixing ratio data were plotted on a Paluch diagram (Paluch 1979) along with smoothed potential temperature and water vapor mixing ratio data from the 01:40 UTC and 01:37 UTC NCAR soundings (refer to Fig. 1.1 for the location of the soundings relative to the storm) in an effort to reveal

possible source regions for the wake air mass in a conserved variable framework. Potential temperature and water vapor mixing ratio, for the purpose of a conserved variable analysis, were treated as being conserved over the period of advection for parcels traveling from the inflow to the RFO. In order for this assumption to be valid for the scales being considered in this analysis, two assumptions were made. First, total water mixing ratio was assumed to be conserved for any parcel as it advected into the RFO. Given that no precipitation was observed by radar along the RFGF to the south of the hook echo, any water vapor lost to cloud water was assumed to evaporate after parcels crossed over the RFGF, thus conserving total water mixing ratio and allowing water vapor mixing ratio to remain unchanged between its pre-condensation and post-evaporation phases. Related to this assumption, diabatic processes which would warm or cool parcels traversing the RFGF were assumed to be fully reversible, thus conserving potential temperature between pre-condensation and post-evaporation phases. For the purpose of the conserved variable analysis, UAS data were subjectively partitioned into four categories: inflow (pre-RFGF environment), initial RFO (RFGF to wake), wake intrusion, and RFIS. The 01:40 UTC sounding showed low altitude data which most closely aligned with UAS data collected in the pre-RFGF air mass (as compared to other soundings launched near the storm).

The wake air mass appears to fall along two mixing lines. The high potential temperature values to the right of the 01:40 UTC sounding line, denoted as red circles (Fig. 3.5), fall between the 01:40 UTC sounding line and the 01:37 UTC sounding lines, suggesting that some of the air in the wake may have been a mixture of the primary RFO and the warmer, moist air mass sampled by the 01:37 UTC sounding near 500-600 m

AGL (Fig. 3.5). A second mixing line appears to lie between the initial RFO and a warmer and drier region at altitudes between 600 and 1000 m in the inflow. It follows from the placement of these two mixing lines that air from above the RFO and originating in the inflow air mass may have penetrated into the wake region.

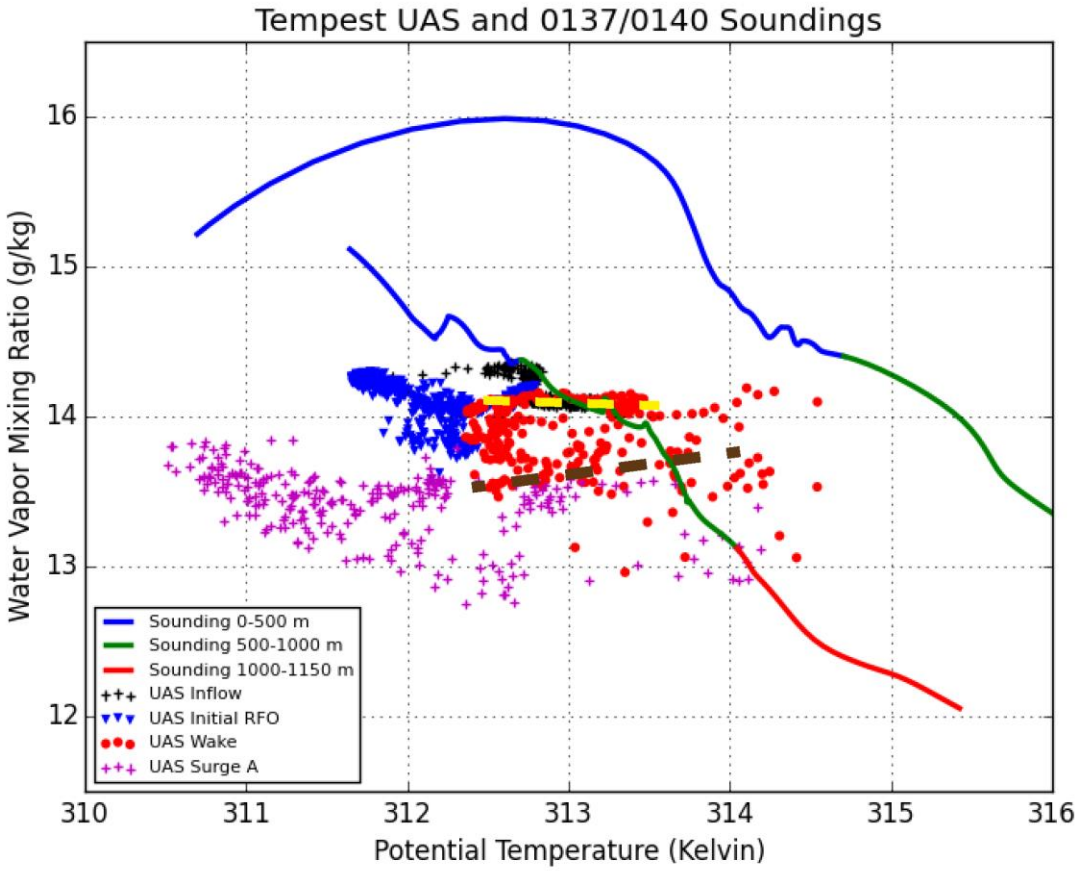

Fig. 3.5: Annotated scatterplot of 01:40 UTC and 01:37 UTC NCAR soundings (01:40 UTC sounding lower left solid line) and Tempest UAS water vapor mixing ratio (gkg^{-1}) and potential temperature (K). Surface sounding values begin at the upper left of the solid sounding line (color coded by height AGL), and end on the bottom right. The yellow dashed line represents a mixing line that a portion of air in the wake appears to fall along, while the brown dashed line represents a second apparent mixing line. Inflow observations were defined by RFGF-relative distances > 0 m, initial RFO by -4230 m < distance < 0 m, wake by -8570 m < distance < -4230, and Surge A (RFIS) by distance < -8570 m.

While it has been established that relatively warmer air infiltrated the RFO above the surface, it does not necessarily follow that a wake intrusion would also be found at

the surface. The scout vehicle for the UAS, which also travelled along a south-north trajectory along Colorado Highway 71, collected similar measurements to the UAS (for specifics on these measurements and subsequent data processing, see Chapter 2.2. Additionally, data from 3 Pennsylvania State University (PSU) mobile mesonets and an array of StickNets (Weiss et al. 2008) (Fig. 3.1) collected *in situ* surface thermodynamic data. Given the spatiotemporal proximity of UAS thermodynamic measurements to surface-based measurements, these datasets are compared to examine vertical continuity (or lack thereof) of the features inferred from UAS data.

The surface observing platforms encountered a similar pre-RFGF environment to that measured by the UAS. Air at the surface was generally warm and moist, with a maximum in potential temperature occurring near 5 km in advance of the RFGF. At distances within a kilometer of the RFGF, the potential temperature was approximately 1 K lower than the maximum at 5 km.

Surface observations collected rearward of the RFGF suggest that the wake and RFIS inferred to exist from UAS data were also present at the surface. However, these features appeared differently at the surface than aloft. An initial drop of ~1 K was recorded as the RFGF crossed the StickNet array. Rearward of this initial cooling, potential temperature measured by the StickNets increased by 1-2.5 K with respect to values before RFGF passage, reaching a maximum at approximately 5 km behind the primary gust front, near where the warming observed by the UAS began but before temperatures aloft reached their maxima (Fig. 3.6). StickNet potential temperature north of 39.67^0 N recorded local maxima in potential temperature closer to the RFGF. In contrast to potential temperature aloft, StickNet-observed potential temperature in the

wake at the surface exhibited a single maximum (Fig. 3.6). In general, as measured by the southern branch of StickNets, potential temperature increased from 0.5-2 K in the 2.5-9 km range rearward of the RFGF (Fig. 3.6). Corroborating this finding, PSU mobile mesonets also observed a local maximum in potential temperature near 39.67^0 N (Fig. 3.7). StickNets along and north of 39.65^0 N recorded a rapid drop in potential temperature between 5 and 10 km rearward of the RFGF. This decrease in potential temperature was likely tied to the RFIS encountered by the UAS. The PSU mobile mesonets encountered a more gradual decrease in potential temperature north of 39.70^0 N, suggesting that the RFIS may not have been as well defined in the northern RFO, or may not have existed at all. If the latter was the case, this would suggest that the RFIS existed as a result of density current wake dynamics, by which the wake acted to erode the RFO such that the trailing portion of the RFO manifested as a RFIS.

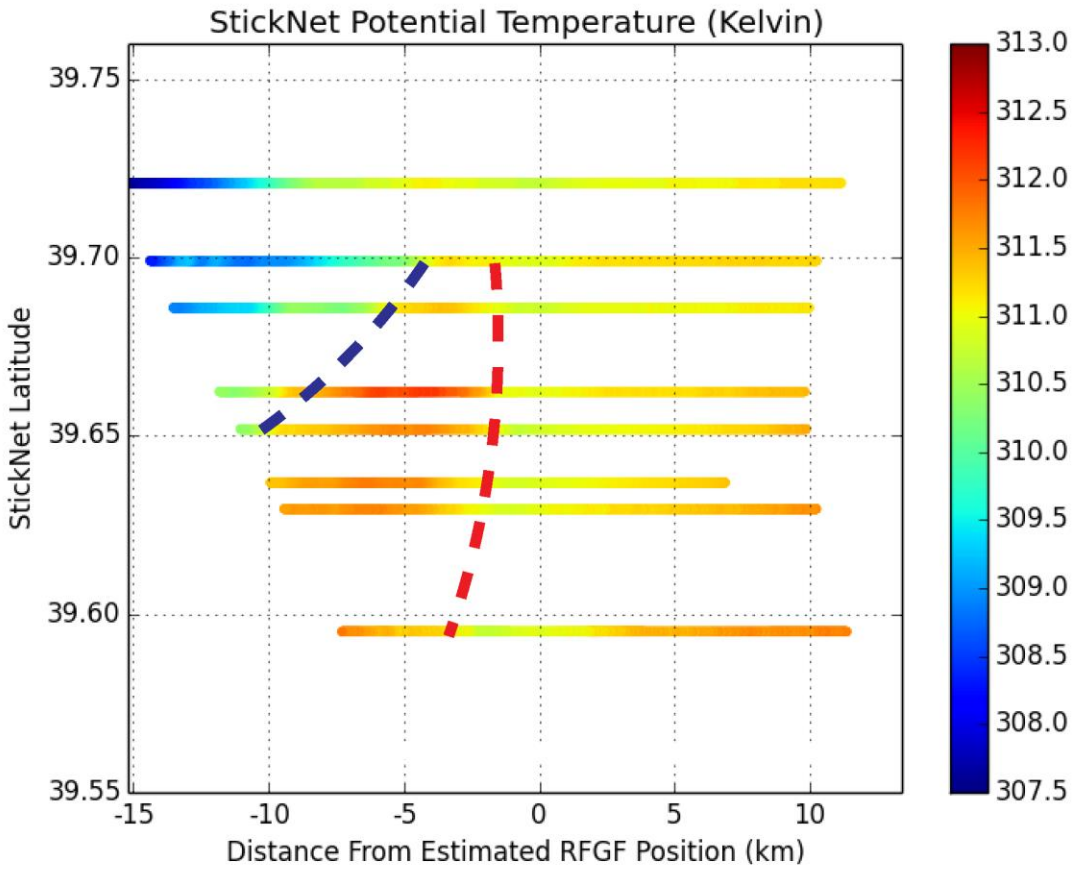

Fig. 3.6: StickNet traces of potential temperature. The blue dashed line denotes the beginning of the RFIS, and the red dashed line shows the beginning of the outflow wake at the surface.

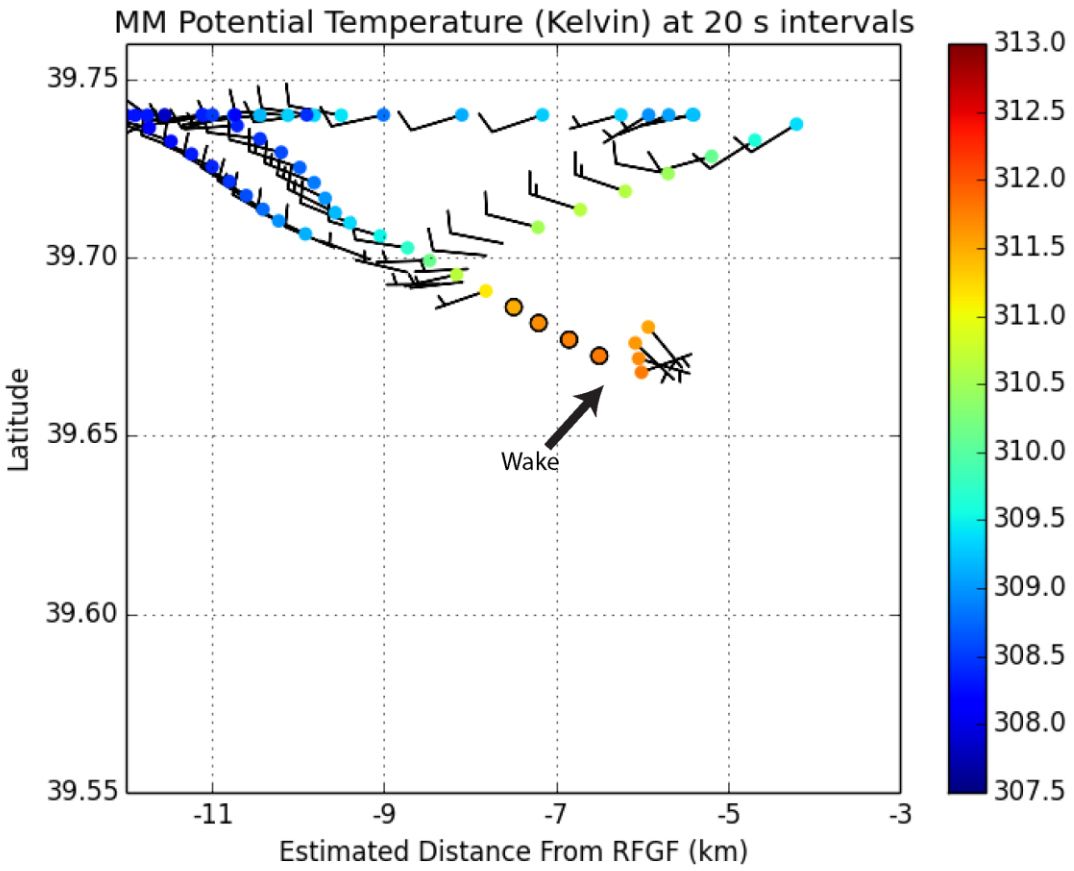

Fig. 3.7: Analysis valid from 01:50-02:00 UTC. Traces from three PSU mobile mesonets (probes 2, 3, and 7). Winds ms^{-1}.

The increase in potential temperature from the primary RFO rearward to the wake was not as rapid as the subsequent cooling in the RFIS. This could be explained by warm air from aloft mixing with air in the primary RFO such that air temperatures only gradually warm as the wake approaches, which would be consistent with the warm air being advected into the outflow through the wake. The larger temperature gradient between the wake and the RFIS may have existed due to kinematic frontogenesis in this region, whereas the temperature gradient behind the RFGF may have been weaker due to surface kinematic frontolysis.

Thermodynamic data collected by the scout mesonet exhibited the same patterns as those collected by the StickNet array. Scout mesonet observations contained some differences in thermodynamic quantities, perhaps due to differences in data collection time or instrumentation response times. However, as seen in Fig. 3.8a, scout mesonet potential temperature observations exhibited a distinct warming near 5 km rearward of the RFGF, and a strong cooling farther back into the outflow, corroborating observations collected by the StickNet array.

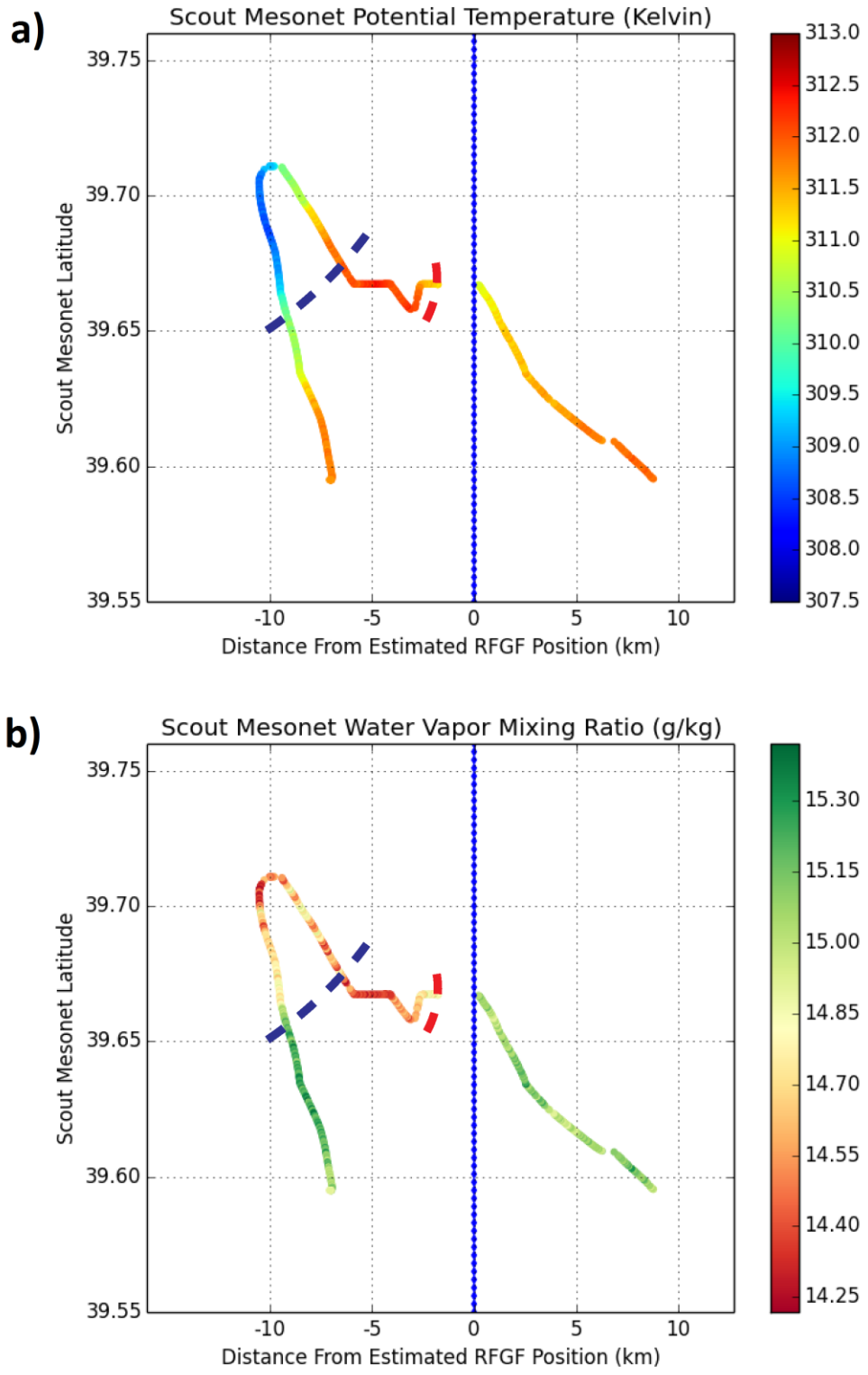

Fig. 3.8: Traces of scout mesonet a) potential temperature and b) water vapor mixing ratio. The blue dashed line represents the drop in potential temperature associated with the RFIS, while the red dashed line denotes the beginning of the outflow wake at the surface.

Scout mesonet water vapor mixing ratio observations exhibited some similarities to those collected by the UAS, though there were also significant differences between the wake region at the surface and aloft (Fig. 3.8b). The primary similarity between surface q_v and q_v aloft was that the RFO was generally drier than the pre-RFGF air mass. The lowest q_v values measured by the scout mesonet were found in the wake. Scout mesonet observations suggested that higher q_v (Fig. 3.8b) may have existed in the second traverse through the wake region.

Surface wind speed and direction data collected by StickNets and mobile mesonets were analyzed in the same RFGF-relative reference frame as the thermodynamic observations. StickNet observations showed generally easterly or northeasterly flow in advance of the RFGF. Winds then shifted to a more westerly or northwesterly direction at the passage of the RFGF. At all but the farthest north StickNet (Fig. 3.9), winds shifted back to easterly and northeasterly between 4-6 km rearward of the RFGF. The southern StickNets maintained an easterly wind component during the remainder of the analysis period. Two of the northern StickNets measured shifts to northwesterly flow at about 10 km rearward of the RFGF. Potential temperature decreased coinciding with the northwesterly wind shift, supporting the wind shift's connection to the cold RFIS. Kinematic observations from the scout mesonet and PSU mobile mesonets generally corroborated the wind field inferred from StickNet data (Figs. 3.7 and 3.10).

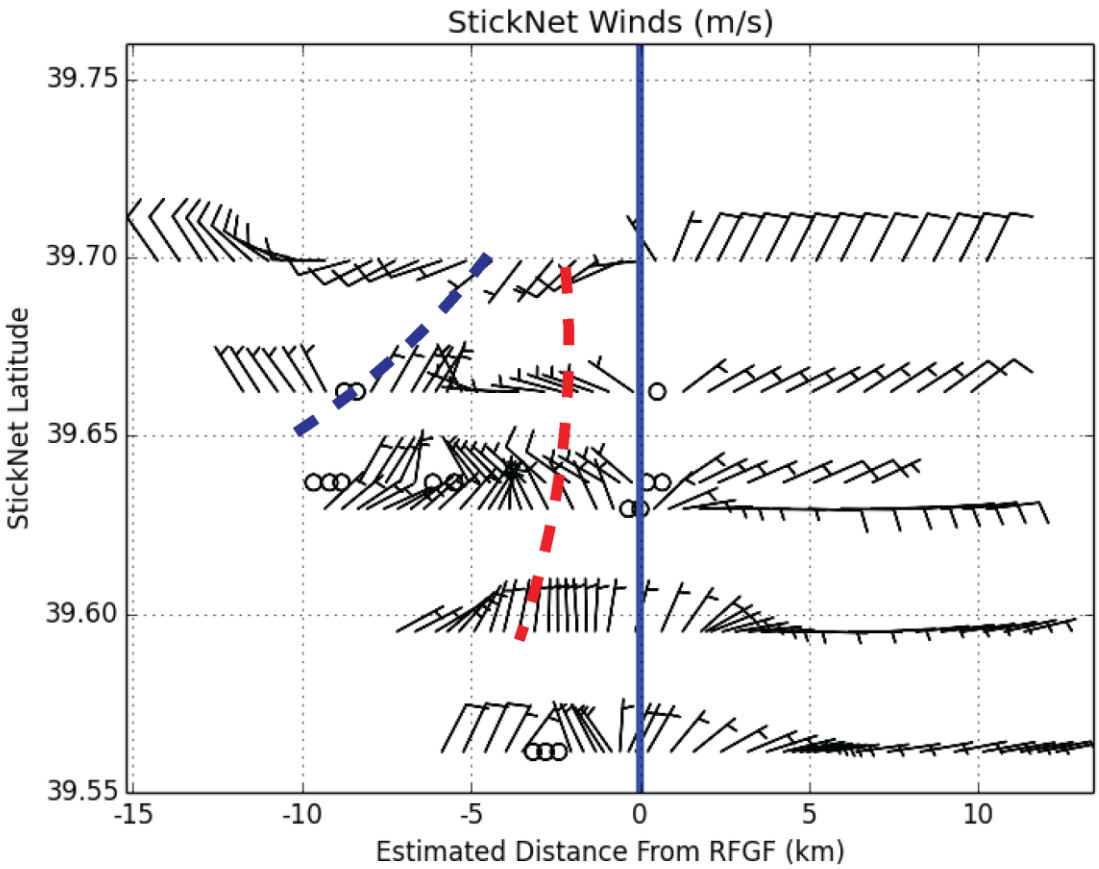

Fig. 3.9: Wind barbs (ms^{-1}) in RFGF-relative frame. As in other figures, the solid blue line represents the RFGF. StickNets which had flagged wind speed or direction were not included.

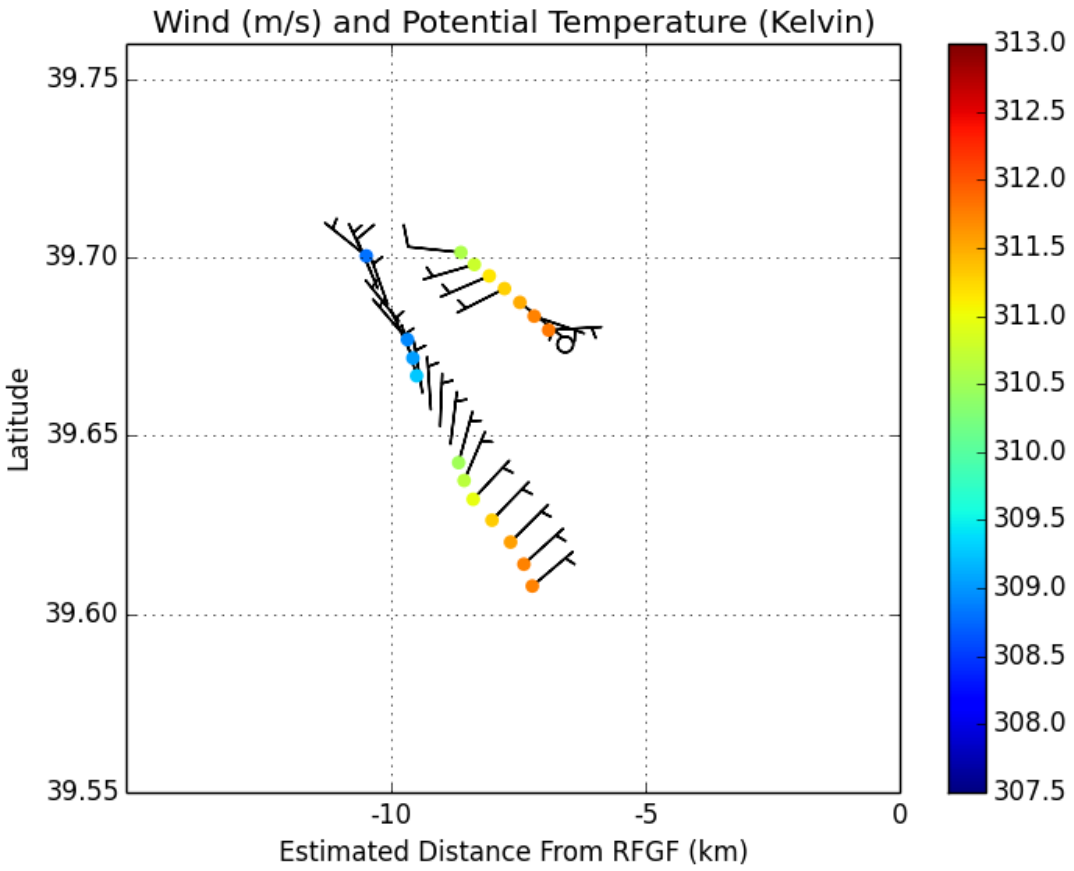

Fig. 3.10: Scout mesonet potential temperature (K) and winds (ms^{-1}).

The wind field measured by StickNets suggested that an area of diffluent flow existed approximately 3-6 km rearward of the RFGF, where winds shifted from northwest to northeast or east-northeast. This region of surface diffluence suggests that a downdraft may have been present 3-6 km rearward of the RFGF. However, farther to the north in the RFO, this diffluent pattern was not present. Rather, winds remained west-southwesterly until a shift to northwesterly winds occurred at ~11 km behind the RFGF (Fig. 3.9). Thus, a possible downdraft extending to or near the surface in the wake was not ubiquitous from south to north through the RFO, but instead was favored in the southern portion of the RFO.

As discussed in Chapter 2.1, NOXP performed shallow volume scans from 1^0-7^0 elevation; these volume scans captured some of the vertical and horizontal flow structure within the RFO, especially from about 01:58 UTC onward, when the RFGF was close enough to NOXP that the vertical structure of the gust front head and flow structure to its west could be examined. Tilts at 1^0 elevation were excluded due to extensive missing data. A few prominent features within the RFO flow field become apparent when viewed on range-height plots derived using 6 elevation tilts (2^0-7^0). First, the RFO possesses an elevated head to the south of the hook echo (as indicated by inbound radial velocity; (Fig. 3.11a,b,c). Second, an extensive area of outbound radial velocity was found rearward of the RFO head (at the same altitude as the inbound velocity at the RFGF). Third, the depth of the RFO (inferred from inbound radial velocity) increased from south to north. For example, at 02:00 UTC, outflow in the southern region of the RFGF appeared to extend to roughly 0.8 km AGL at its highest point, whereas outflow depth appeared to exceed 1 km closer to the hook echo (Fig. 3.11a). Over the 02:00-02:08 UTC period, the outflow in the northern RFO extended from the surface to at least 1 km, while the outflow in the southern RFO appeared to be no deeper than 0.8 km. Fourth, in areas of shallower outflow, a region of radial divergence was found at the rear of the elevated outflow head. This area of radial divergence is consistent with the *in situ* observations of surface divergence and the inferred attendant downdraft which could advect and mix inflow air (located above the density current) with outflow air. The presence of outbound radial velocity in the wake and at the top of the RFGF suggests that winds in these regions had a significant easterly component, given NOXP's location to the east of the RFGF. Finally, these features were persistent: they were found in 5 volumes covering a 10 minute period.

The persistence of these features also lends confidence to the assumption that the UAS and surface observing platforms encountered the structures seen in NOXP data, much of which was collected from 5-15 minutes after the *in situ* data collection periods presented previously.

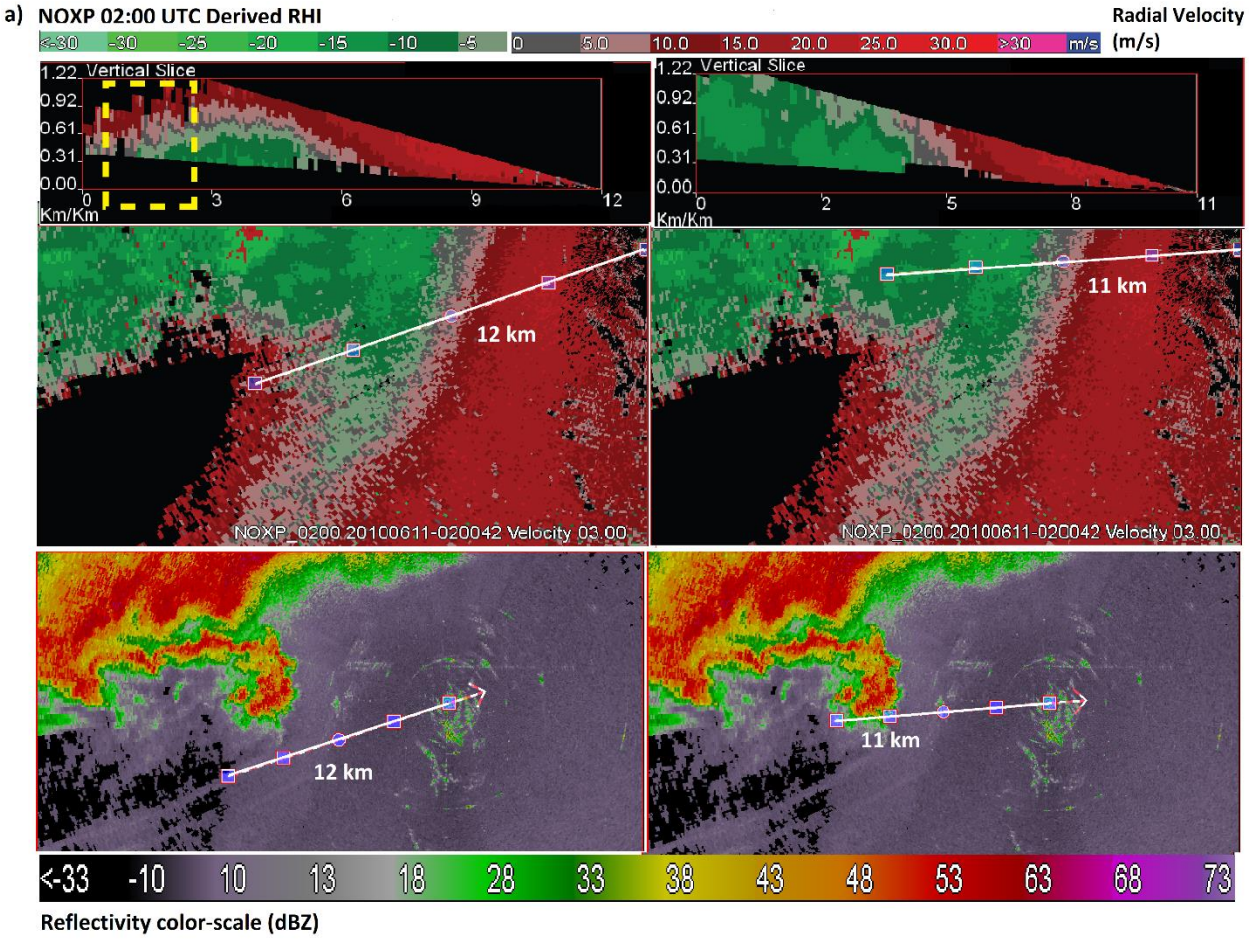

b) NOXP 02:04 UTC Derived RHI

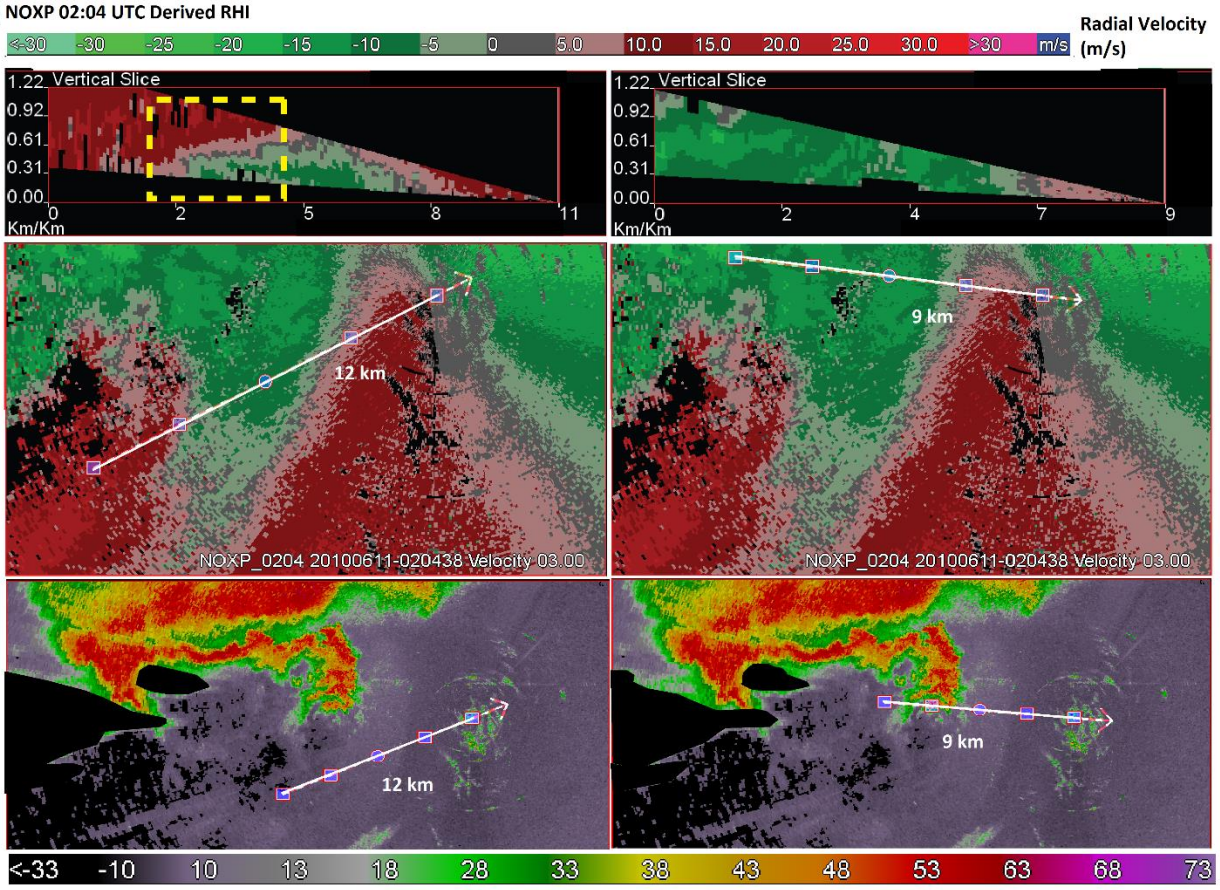

Reflectivity color-scale (dbZ)

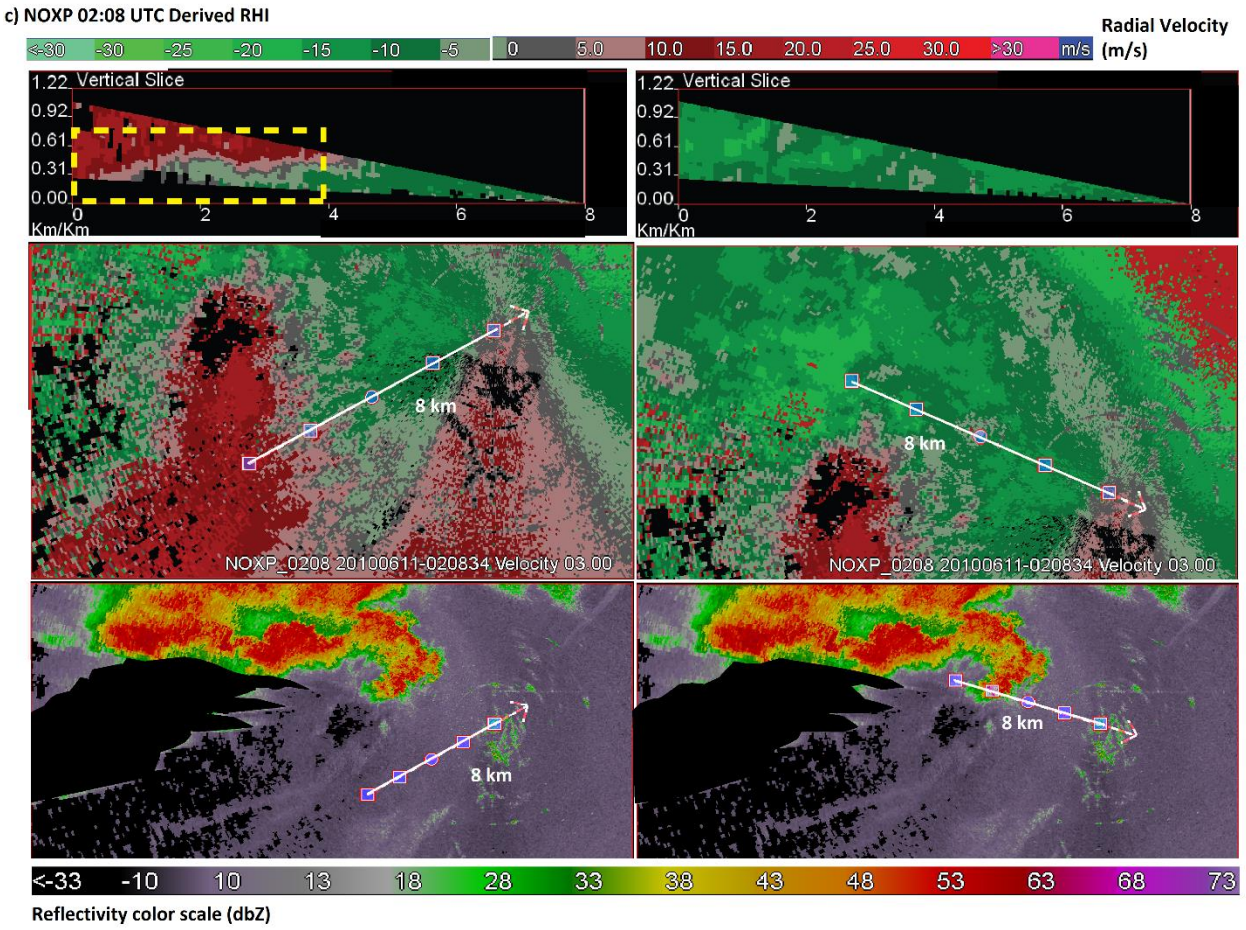

Fig. 3.11: Vertical cross sections of radial velocity from NOXP. Cross sections are in pairs, from top to bottom, at a) 02:00 UTC, b) 02:04 UTC, and c) 02:08 UTC. Yellow dashed box represents region of radial divergence.

Chapter 4
Discussion

The Last Chance, Colorado supercell exhibited an RFO which expanded to the east over time through the period of focus. Within the expanding RFO, multiple thermodynamic and kinematic in-homogeneities existed. The Tempest UAS, surface observation platforms, and a Doppler radar provided evidence that the RFGF was shallower to the south of the supercell's hook echo, and that the RFGF may have become

mostly or fully detached from the rest of the RFO during a non-tornadic phase of the supercell, particularly in southern areas of the RFO. In the wake of the RFGF, relatively weak ground-relative winds with a strong easterly component were found, which contrasted with the primarily westerly, southwesterly, or northwesterly winds in the initial outflow and outflow near the hook echo. Easterly ground-relative winds were found, generally, from about 4-9 km to the west of the RFGF. In this region of easterly wind, potential temperature values increased by up to 2 K (with respect to temperatures found in the primary RFO). Increased potential temperature was also found east of the wind shift, suggesting that a warm downdraft likely existed somewhere from 4-6 km rearward of the RFGF, near where the wake of a density current was found. Scout mesonet and UAS observations showed relatively dry air in the wake (compared to pre-outflow air and the initial RFO), suggesting that dry air had been mixed into the wake, likely from inflow air located above the outflow. The 01:40 UTC NCAR sounding showed that potential temperature increased with altitude, while water vapor mixing ratio decreased with altitude over the lowest 1150 m, suggesting that a warm and dry air mass likely would originate in the inflow. However, scout mesonet observations from farther south in the wake suggested that more moist air was present. Considering that the water vapor mixing ratio field measured by the UAS was quite variable in the wake, it appears likely that the RFO was turbulent aloft and that the air comprising the wake came from both the pre-RFGF air and air from the initial RFO.

Range-height cross sections derived from NOXP PPI scans suggested that an area of radial divergence existed 4-6 km rearward of the RFGF to the south of the flared-out hook echo. It is possible that a downdraft existed about 4 km rearward of the RFGF, such

that air from above the RFGF and pre-RFGF air advected over the density current head could have been advected downward to the ground, resulting in the diffluent surface wind pattern seen in StickNet data and the warm potential temperature discussed previously. In range-height plots at 02:00 UTC and 02:04 UTC (Fig. 17a,b), radial divergence behind the RFGF appeared to be stronger at low levels, indicating that a downdraft could have existed here. The presence of weak wind fields in the wake (as some mobile mesonet observations and StickNet observations showed nearly calm winds in the wake) could indicate that parcels being advected downward through the wake may have had a level of neutral buoyancy well above the ground, such that their vertical velocity by the time they reached the surface was near zero. The lack of a strong downdraft near the surface layer could explain the lack of a momentum surge in the wake. Unfortunately, given the lack of dual-Doppler observations at the RFGF, it is impossible to state with certainty where the air in the wake came from. However, given the relatively consistent thermodynamic and kinematic observations collected behind the RFGF, it seems probable that air in the wake aloft penetrated to the surface at times, and that the air in the wake included a mixture of inflow air and air from above the gust front, both of which would be warmer than the initial RFO and the RFIS.

Theoretical and observational justification for mixing of warm air into an RFO via a density current wake are based on the presence of Kelvin-Helmholtz Instability (KHI), a shearing instability that exists near the upper interface of many density currents (Simpson 1980; Simpson 1997). Given the low vertical resolution of NOXP data and a lack of full three-dimensional wind components aloft, the Richardson number was not estimated, as has been done by previous studies. However, if Kelvin-Helmholtz billows

were responsible for the presence of a deep outflow wake, it would be expected that relatively turbulent flow would have existed in the RFO, particularly near the rear edge of the initial RFO. A subjective analysis of spectrum width measured by NOXP was undertaken to determine the character of turbulence within the RFO as compared to pre-RFGF flow. Generally, spectrum width was larger in the initial RFO than in advance of the RFGF (Fig. 4.1). Moreover, spectrum width tended to increase near the rear of the initial RFO (near the beginning of the outflow wake) (Fig. 4.1). Given the vertical shear in NOXP radial velocity (Fig. 3.11) and the larger spectrum width in the RFO compared to the inflow (Fig. 4.1), it is assumed that KHI was supported. Large KHI billows can form to the rear of the head of a density current and occupy much of the depth of the density current in the wake (Simpson 1980; Droegemeier and Wilhelmson 1987; Xue et al. 1997; Geerts et al. 2006). Air with the thermodynamic and kinematic properties of the surrounding environment may be mixed into the density current, possibly resulting in relatively warm air reaching the surface and (given vertical shear opposite to the propagation of the density current) ground-relative surface winds opposite the propagation of the density current in the wake. In order for environmental air to be drawn downward through the wake of a density current, mass divergence at low levels may also aid in drawing down parcels from above the outflow.

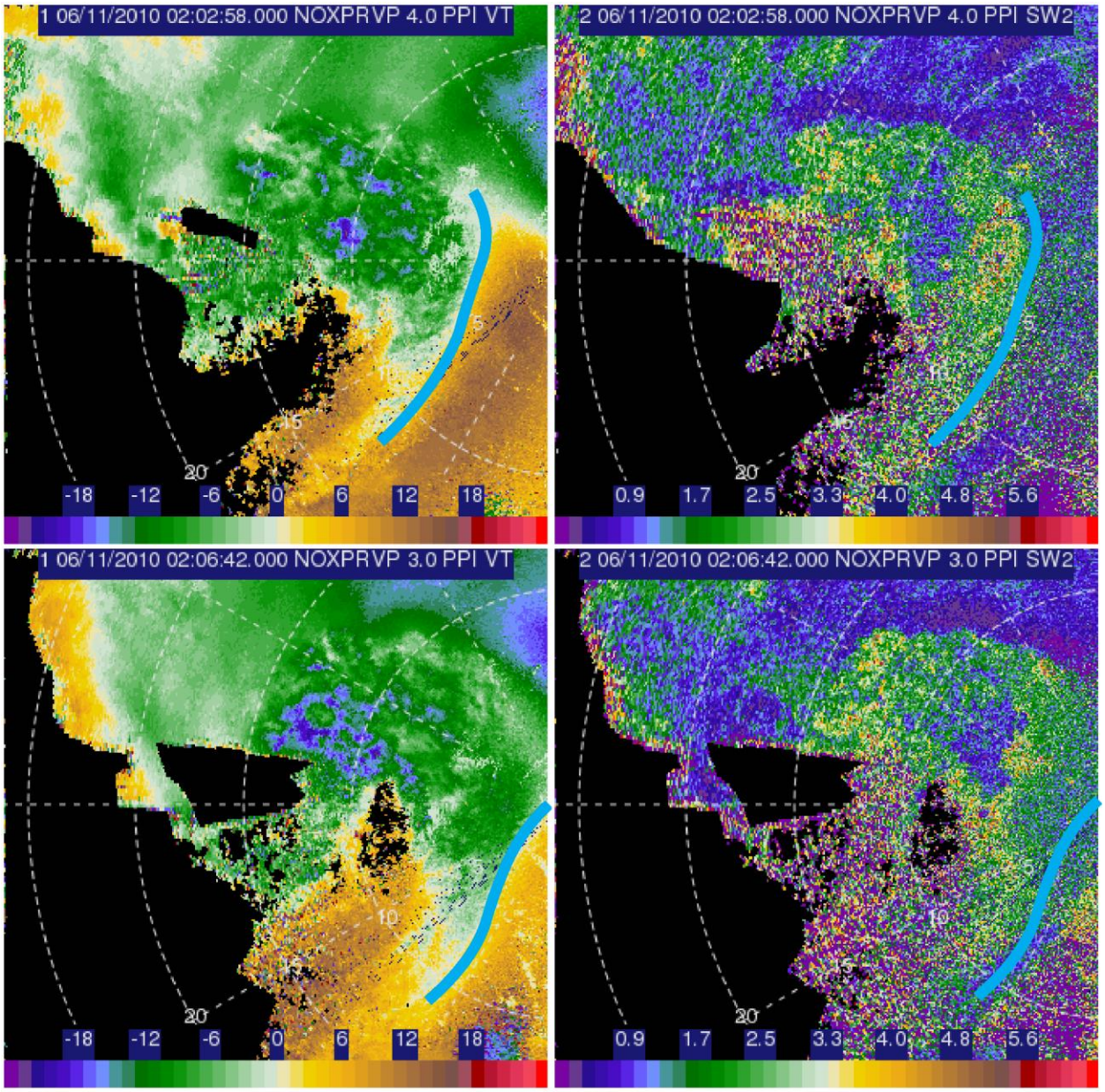

Fig. 4.1: Radial velocity (ms^{-1}) (left) and spectrum width (ms^{-1}) (right) at ~02:03 UTC and ~02:07 UTC. White dashed rings are spaced every 5 km.

It is hypothesized that a turbulent wake extended, at least periodically, to the ground, cutting off the main body of the RFO from the leading edge of the outflow. This cutoff seems to have occurred to the south of the hook echo in southern parts of the RFO, but not in the outflow immediately south of the hook echo. The southern RFO appeared to have been shallower than near the hook echo, which could make it easier for positively

buoyant parcels to penetrate through the outflow to the surface. A possible explanation for why the RFO appeared to be shallower in its southern extent is that, simply, the outflow became farther away from its cold air source with southern extent (Xu and Moncrieff 1994).

While thermodynamic observations support the presence of an RFIS, kinematic observations do not follow a model for any RFIS that has been presented previously. The definition of an RFIS introduced by Lee et al. (2012) requires a 13 m s^{-1} increase in wind speed associated with the RFIS. However, the winds in the RFIS observed herein increased by only 5 ms^{-1} and were principally manifest as a wind shift. The observed wind field manifestation of the RFIS is consistent with a mechanism proposed to explain the RFIS formation: the RFIS is not a "surge" in the RFO per se, but the trailing portion of the RFO that has been cut off from the outflow head by the wake. Importantly, like RFIS fitting the Lee et al. definition, the RFIS boundary observed here was characterized by confluence (and likely convergence). Thus a line of kinematic frontogenesis can be created by this mechanism at the interface between the rear of the wake and the RFIS where easterly flow shifts to westerly or northwesterly flow. Recall that the observed RFIS boundary was capable of supporting a strong leading-edge updraft, which would support the presence of low level convergence.

As discussed in Chapter 1.1, RFIS have been hypothesized to aid in tornadogenesis and tornado intensification due to their ability to provide increased surface/near-surface convergence within an established RFO. The surface convergence that can exist in association with an RFIS boundary formed as proposed here could serve the same function. However, an important caveat exists when trying to attribute an

increased likelihood for tornadogenesis or tornado intensification to the presence of an RFIS boundary formed by this mechanism. This process is more likely to occur away from sources of cold air (i.e., south of the hook echo). Thus, convergence along the secondary boundary would seem unlikely to impact the surface circulation center near the hook unless the RFO is uniformly shallow.

Independent of whether or not the resultant RFIS boundary could aid in tornadogenesis through stretching, the presence of relatively warm air in the RFO is also potentially important for tornadogenesis. The associative relationship between cold pool buoyancy and tornadogenesis (Markowski et al. 2002; Markowski 2002; Grzych et al. 2007; Hirth et al. 2008; Lee et al. 2012) may be attributable to the resistance of negatively buoyant air within the cold pool to vertical acceleration (Markowski and Richardson 2014). Thus, an RFO warmed through advection/mixing of inflow air in a penetrating wake circulation could substantially reduce the stability of the RFO air near the surface circulation.

Can the mixing of warm air into an RFO through the outflow wake result in warm air residing near the surface circulation, thus increasing the likelihood of tornadogenesis? In the case presented here, easterly ground-relative momentum was only found at the surface in southern portions of the RFO, and the warming in the wake of the RFGF was tempered or non-existent north of 39.7^0 N. This was hypothesized to be a consequence of deeper outflow to the north near the hook echo. Thus, the outflow would need to be shallower for the wake circulation to advect inflow air into the RFO near the circulation center. Alternatively, warm air in the wake farther to the south could be advected northward toward the mesocyclone by any winds with a strong southerly component in

the RFO. This would require inflow with a more southerly storm-relative wind component than existed in this case.

The potential importance of warm air reaching the surface in the wake region of an RFO calls into question how common of a process this may be in supercells. In a dual-Doppler study of vertical circulations in a cold front, Geerts and co-authors found that a downdraft existed rearward of the cold front head (Geerts et al. 2006) which may have advected pre-frontal air downward to the surface. The downdraft in the wake in their study, similar to previous modelling studies (Drogemeier and Wilhelmson 1987; Limpert 2013), appeared to be co-located with a large Kelvin-Helmholtz billow which acted to either partially or fully cut off the main body of the density current from the leading head. While it is hypothesized in the Last Chance study that a breaking Kelvin-Helmholtz billow was responsible for the presence of warm air near and at the surface in the Last Chance case, it is difficult to say how common of an occurrence this may be. In a set of model simulations investigating the effect of stratification on density current structure, Liu and Moncrieff found that large low-level stratification can promote deep penetration of inflow air into a cold outflow (Liu and Moncrieff 2000). Recall that the UAS and 01:37 UTC (southernmost) sounding captured some boundary layer stratification. It appears that density current depth (which was inferred from NOXP radial velocity data) may have played a large role in whether a wake could circulate air from aloft to the surface. Previous studies (e.g. Xu and Moncrieff 1994) have found that low-level shear plays a role in the depth of a density current. Specifically, all else held constant, a density current should be shallower if the environmental shear vector in the layer occupied by the density current is pointed towards the cold air. Given that the RFGF propagation was

from west to east, the shear of the u-component of the environmental wind east of the storm was analyzed in order to determine the direction of the low-level shear vector with respect to the cold pool propagation.

Wind data from three soundings (Fig. 4.2) launched to the east of the supercell (refer to Fig. 1.1 for the locations of the soundings) were analyzed to evaluate the vertical shear of the u-component of the horizontal wind in the boundary layer. The RFO propagated generally from west to east, so $\frac{\partial u}{\partial z}$ was used to approximate the component of the vertical wind shear perpendicular to the RFGF.

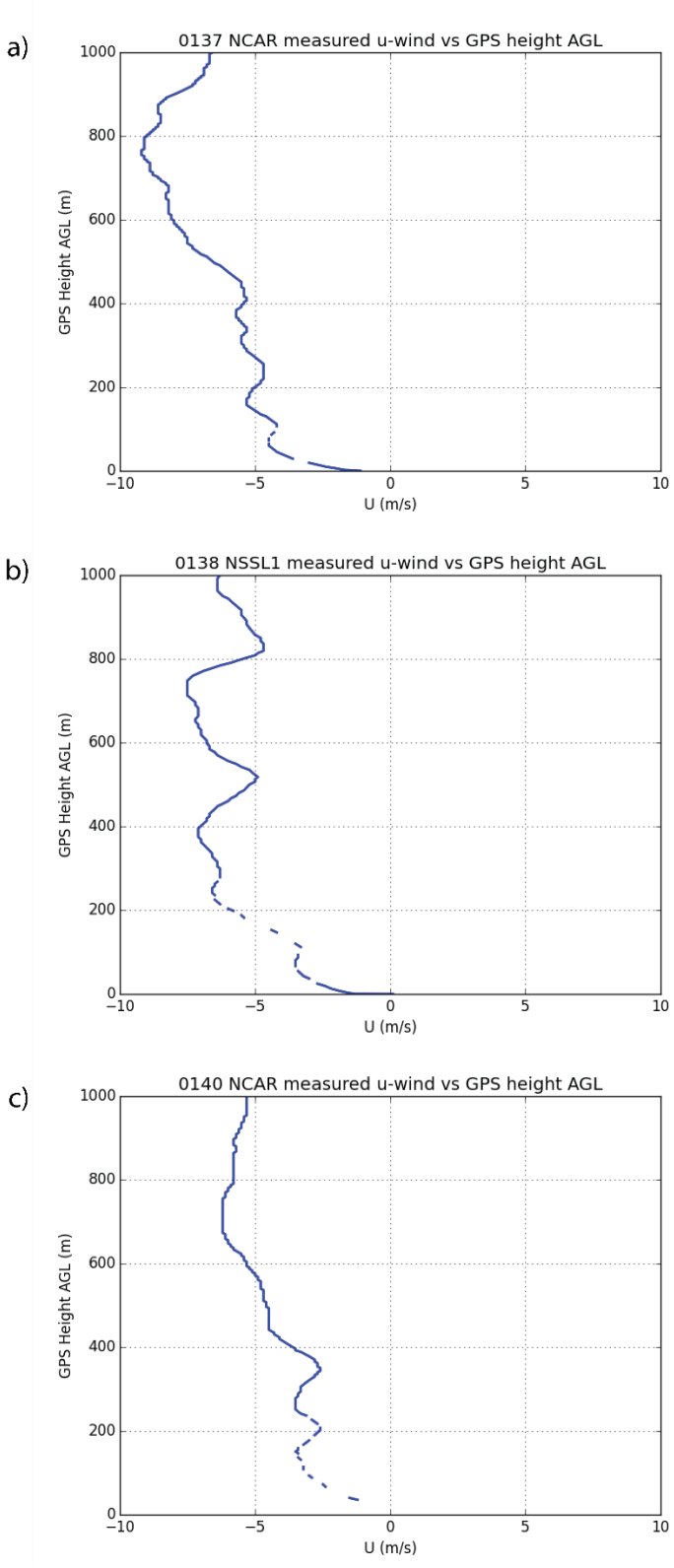

Fig. 4.2: U component of wind (ms^{-1}) from a) 01:37 UTC, b) 01:38 UTC, and c) 01:40 UTC soundings.

The value of $\frac{\partial u}{\partial z}$ in the lowest 750-1000 m of the boundary layer was generally negative (Fig. 4.2); that is, the low-level shear vector was pointed towards the cold side of the density current. All else held equal, this shear orientation should lead to a shallower density current, and according to the results of Xue et al. 1997, perhaps larger and deeper Kelvin-Helmholtz billows. Moreover, the ground-relative easterly flow found in the boundary layer in advance of the RFGF could also have acted to accelerate surface flow in the RFO to the west (where and if parcels with easterly momentum were mixed to the surface). As was seen in some StickNet and mobile mesonet observations, weak easterly flow could be found in some areas where warming under the outflow wake also occurred.

Chapter 5

Conclusions

The Tempest UAS, NOXP, StickNets, scout mesonet, and several PSU mobile mesonets sampled the RFO of the 10 June 2010 Last Chance, Colorado supercell during a non-tornadic phase. During this sampling, StickNets primarily sampled the southern RFO, mobile mesonets the northern RFO near the flared-out hook echo, and the scout mesonet and Tempest UAS a north-south transect through the RFO. The suite of observing platforms sampled the pre-RFGF air mass, RFGF, a turbulent wake, and rear-flank internal surge (RFIS) over a 36 minute span, with NOXP data adding an additional 6 minutes to the end of the analysis period.

The following tentative conclusions are made and are summarized in Figs. 5.1, 5.2, and 5.3. First, warm air (relative to the initial RFO and RFIS) was found from 4-9 km to the rear of the southern sections of the RFGF (Fig. 5.1). The magnitude of the warming was more pronounced aloft (~3-4 K in some areas) than at the surface. This warmer air was likely entrained into the RFO in the wake of the RFO head, and likely contained a mixture of warm, dry pre-RFGF air with RFO air. Second, surface wind measurements collected by StickNets and mobile mesonets exhibited a diffluent pattern from roughly 4-6 km to the rear of the RFGF, suggesting the possible presence of a downdraft associated with the wake. Range-height plots of radial velocity from 2 minute NOXP PPI scans revealed a region of radial divergence about 4-6 km rearward of the RFGF at heights as low as near 300 m AGL. This radial velocity distribution would be consistent with a downdraft forming about 4-6 km to the rear of the RFGF, which is where diffluent surface winds were found by the StickNets. The altitude at which outbound radial velocity rearward of the RFGF could be found increased with latitude, suggesting that the outflow was deeper closer to the hook echo and that a northward-pointed gradient in outflow depth may have existed. Since the diffluent surface wind pattern (and easterly flow) was less common farther to the north, it is possible that deeper outflow there precluded the wake from extending to the surface (Fig. 5.3). Three of the soundings launched to the east of the supercell suggested that, all else held equal, the environmental shear profile in the boundary layer should have favored a shallow density current. The RFIS appeared to manifest as the arrival of the trailing rear-flank outflow rearward of warming associated with the outflow wake (Fig. 5.2). The presence of relatively cold air at 10 km or farther rearward in the RFO to the north of the suspected

RFO cutoff leaves open the possibility that the secondary outflow surge encountered by the UAS may have existed independent of any processes taking place in the RFGF wake. Thus, it cannot be concluded that the cutting off of the head of the RFO led directly to the formation of a cold RFIS. To the extent that the author is aware, relatively warm air in RFOs has not been directly attributed to the effects of Kelvin-Helmholtz billows in RFO wakes. It does not necessarily follow that the process described above is unusual in supercells, though it may be less common closer to regions where latent chilling may be common (such as some hook echoes).

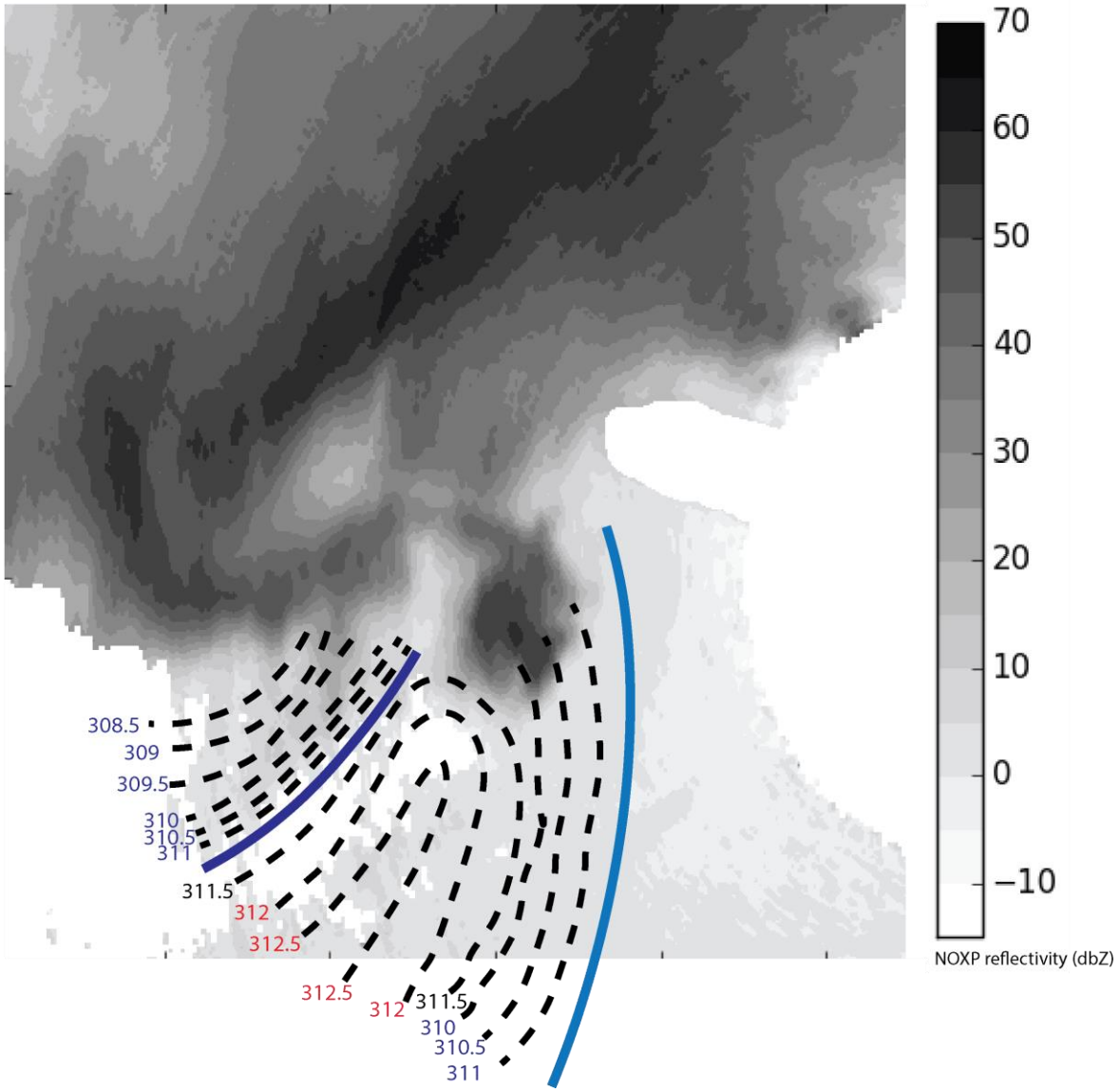

Fig. 5.1: Plan view of surface thermodynamic structures overlaid on 1.1 km NOXP reflectivity factor constant altitude planned position indicator at 01:55 UTC. The solid light blue line represents the RFGF, while the dark blue line represents the RFIS. Dashed lines are isentropes (K).

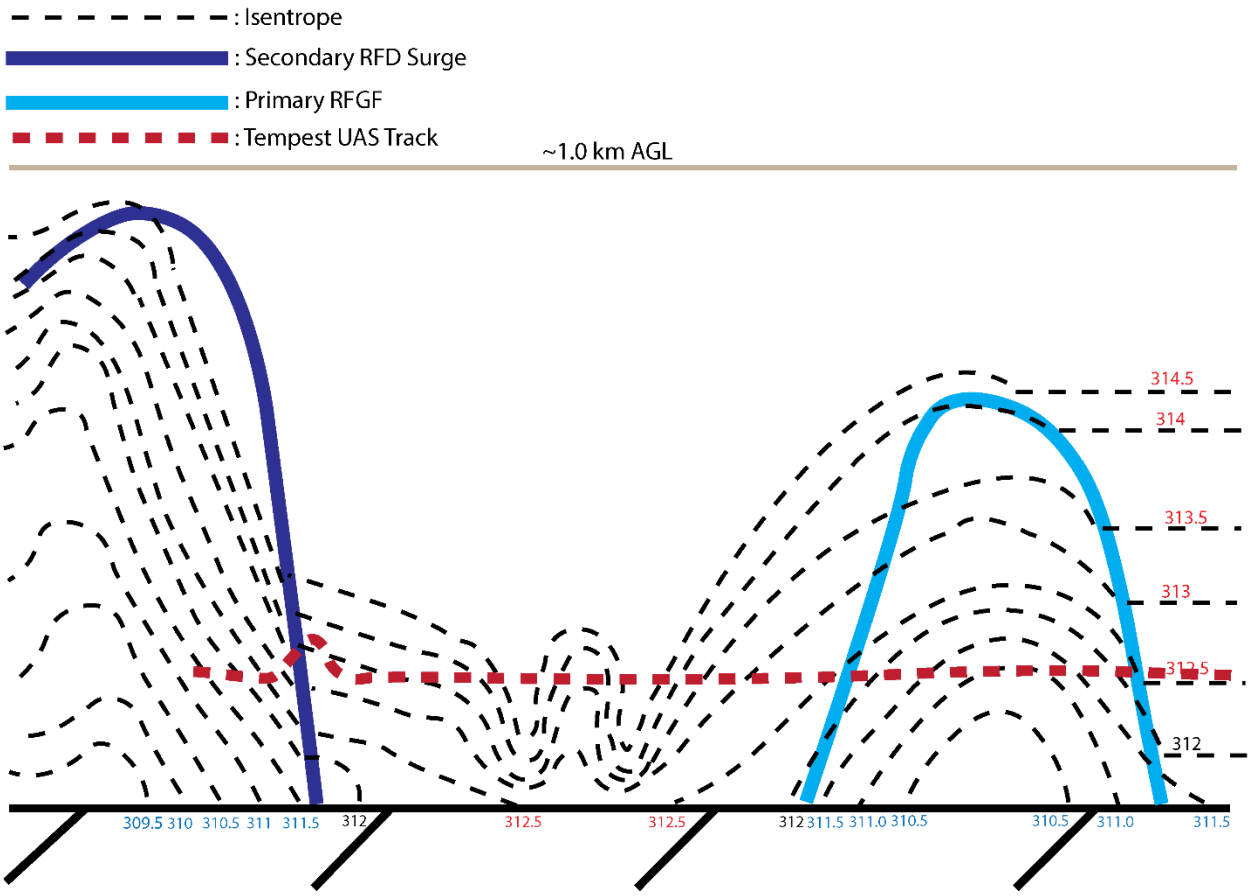

Fig. 5.2: Conceptual model of cut-off RFO with isentropes (K) labeled.

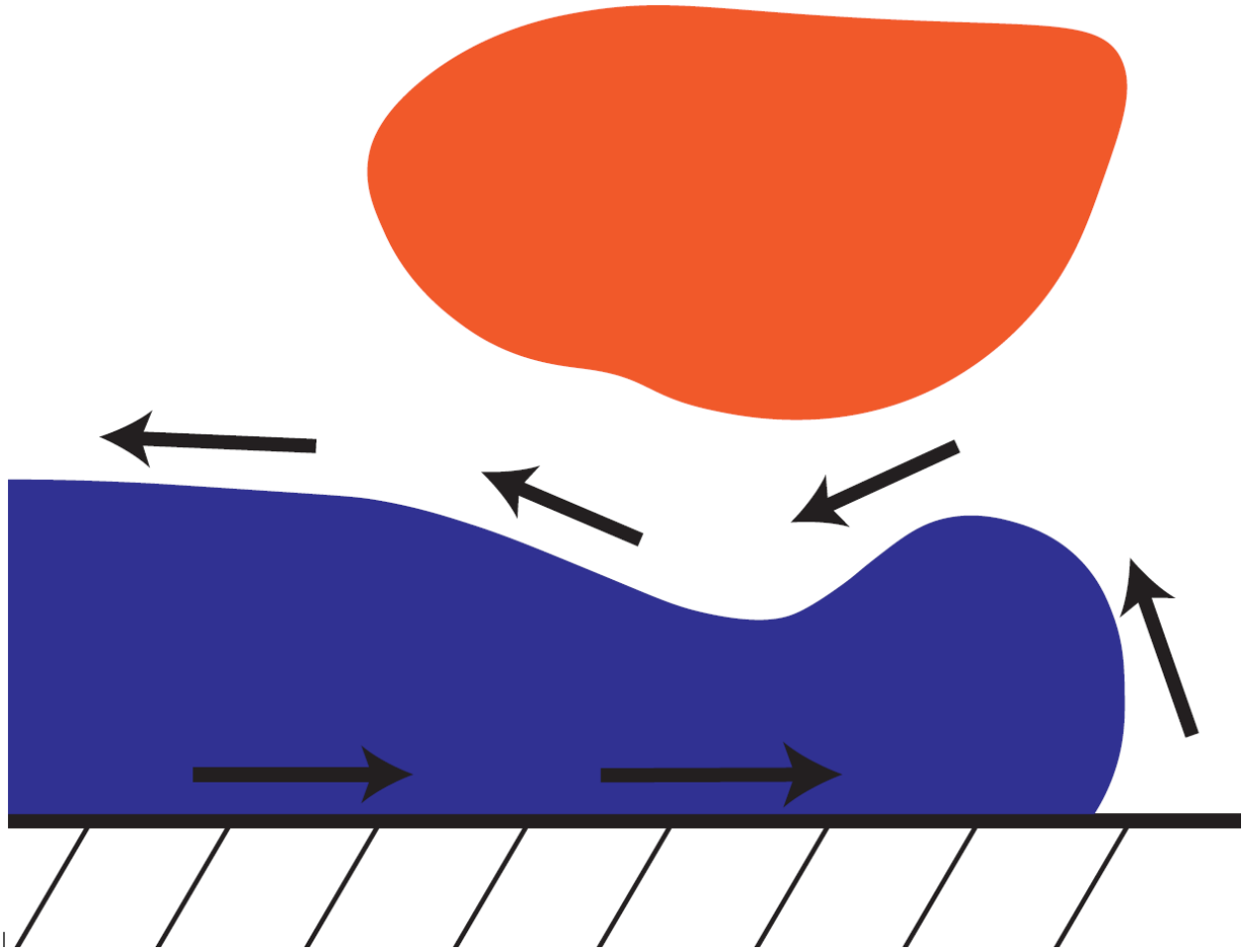

Fig. 5.3: Hypothesized thermodynamic and kinematic structure of northern RFO. Orange represents warm and dry air above the RFO. Blue represents relatively cold outflow air.

The cold outflow surge sampled in this dataset, as discussed previously, does not fit the definition of an RFIS posed by Lee et al. (2012), where a 13 ms^{-1} or greater acceleration in wind *speed* must exist. While most surface platforms observed a northwesterly or westerly wind shift in the region which the UAS measured a significant drop in equivalent potential temperature, there was not a consistent signal for a rapid increase in wind *speed*. However, if RFIS are important for tornadogenesis due to a propensity to help to converge vertical vorticity, an RFIS manifested as a low-level wind shift associated with outflow wake dynamics may yet be important for convergence within the RFO in some cases, given that it occurs close enough to the mesocyclone to

have an effect on the vorticity budget in a developing low-level mesocyclone. Moreover, if the wake was to advect inflow air into the rear-flank outflow close enough to the mesocyclone, this may have the added effect of reducing the thermal stability of low-level parcels which may be ingested by the low-level mesocyclone, which may make tornadogenesis more likely to occur.

Since much of the thermodynamic analysis presented was based on data collected by either stationary (StickNet) platforms or instruments which only performed a single transect through parts of the RFO (UAS and scout mesonet), no attempt to diagnose temporal variability in thermodynamic and kinematic RFO characteristics was made. Finally, the effect that warmer air in the RFO may have had on the evolution of this particular supercell is unknown. The extent to which it is common for 1) relatively warm air to entrain into rear-flank outflows via density current dynamics and 2) a cold RFIS to form by this mechanism cannot be ascertained by this dataset alone. Future work aiming to investigate these questions should attempt to collect and utilize larger datasets of UAS and mobile mesonet RFO transects to gauge the variability in vertical outflow thermodynamic structure.

Bibliography

Beck, J. and C. C. Weiss, 2013: An Assessment of Low-Level Baroclinity and Vorticity within a Simulated Supercell. *Mon. Wea. Rev.*, **141**, 649–669.

Biggerstaff, M. I. and Coauthors, 2005: The Shared Mobile Atmospheric Research and Teaching Radar: A Collaboration to Enhance Research and Teaching. *Bull. Amer. Meteor. Soc.*, **86**, 1263–1274.

Bluestein, H. B., J. B. Houser, M. M. French, J. C. Snyder, G. D. Emmitt, I. PopStefanija, C. Baldi, and R. T. Bluth, 2014: Observations of the Boundary Layer near Tornadoes and in Supercells Using a Mobile, Collocated, Pulsed Doppler Lidar and Radar. *J. Atmos. Oceanic Technol.*, **31**, 302–325.

R. Davies-Jones, 2008: Can a Descending Rain Curtain in a Supercell Instigate Tornadogenesis Barotropically? *J. Atmos. Sci.*, **65**, 2469–2497.

Davies-Jones, R. P., and H. E. Brooks, 1993: Mesocyclogenesis from a theoretical perspective. *The Tornado: Its Structure, Dynamics, Prediction, and Hazards*, Amer. Geophys. Union, 105-114.

Elston, J. S., J. Roadman, M. Stachura, B. Argrow, A. L. Houston, and E. W. Frew, 2011b: The Tempest unmanned aircraft system for *in situ* observations of tornadic supercells: Design and VORTEX2 flight results. *Journal of Field Robotics*, **28,** 461-483.

Geerts, B., R. Damiani, and S. Haimov, 2006: Finescale Vertical Structure of a Cold Front as Revealed by an Airborne Doppler Radar. *Mon. Wea. Rev.*, **134**, 251–271.

Grzych, M. L., B. D. Lee, and C. A. Finley, 2007: Thermodynamic Analysis of Supercell Rear-Flank Downdrafts from Project ANSWERS. *Mon. Wea. Rev.*, **135**, 240–246.

Halbert, K. T., W. G. Blumberg, and P. T. Marsh, 2015: "SHARPpy: Fueling the Python Cult". Preprints, 5th Symposium on Advances in Modeling and Analysis Using Python, Phoenix AZ.

Hirth, B.D., J. L. Schroeder, and C. C. Weiss, 2008: Surface Analysis of the Rear-Flank Downdraft Outflow in Two Tornadic Supercells. *Mon. Wea. Rev.*, **136**, 2344–2363.

Klees, A., Y. Richardson, and P. Markowski, 2014: Preliminary Analysis of the 10 June 2010 Supercells Intercepted by VORTEX2 Near Last Chance, Colorado. *27th Conf. on Severe Local Storms*, Madison, WI, *Amer. Meteor. Soc.*, **P12.164**.

Kosiba, K., J. Wurman, Y. P. Richardson, P. M. Markowski, P. Robinson, and J. Marquis, 2013: Genesis of the Goshen County, Wyoming, Tornado on 5 June 2009 during VORTEX2. *Mon. Wea. Rev.*, **141**, 1157–1181.

Lee, B.D., C. A. Finley, and C. D. Karstens, 2012: The Bowdle, South Dakota, Cyclic Tornadic Supercell of 22 May 2010: Surface Analysis of Rear-Flank Downdraft Evolution and Multiple Internal Surges. *Mon. Wea. Rev.*, **140**, 3419–3441.

Lee, B.D., C. A. Finley, and T. M. Samaras, 2011: Surface Analysis near and within the Tipton, Kansas, Tornado on 29 May 2008. *Mon. Wea. Rev.*, **139**, 370–386.

Lee, B.D., C. A. Finley, and P. Skinner, 2004: Thermodynamic and Kinematic Analysis of Multiple RFD Surges for the 24 June 2003 Manchester, SD cyclic tornadic supercell during Project ANSWERS 2003. *22nd Conf. on Severe Local Storms*, Hyannis, MA, *Amer. Meteor. Soc.*, **P11.2**.

Limpert, G., 2013: Mesovortex Genesis. *Ph.D Thesis*, Department of Earth and Atmospheric Sciences, University of Nebraska-Lincoln, in preparation. Available at http://digitalcommons.unl.edu/geoscidiss/39/.

Liu, C. and M. W. Moncrieff, 2000: Simulated Density Currents in Idealized Stratified Environments. *Mon. Wea. Rev.*, **128**, 1420–1437.

Markowski, P. M., E. N. Rasmussen, J. M. Straka, R. Davies-Jones, Y. P. Richardson, and R. J. Trapp, 2008: Vortex lines within low-level mesocyclones obtained from pseudo-dual-Doppler radar observations. *Mon. Wea. Rev.*, **136**.

Markowski, P.M, J. M. Straka, and E. N. Rasmussen, 2002: Direct Surface Thermodynamic Observations within the Rear-Flank Downdrafts of Nontornadic and Tornadic Supercells. *Mon. Wea. Rev.*, **130**, 1692–1721.

Markowski, P.M., and Y. P. Richardson, 2014: The Influence of Environmental Low-Level Shear and Cold Pools on Tornadogenesis: Insights from Idealized Simulations. *J. Atmos. Sci.*, **71**, 243–275.

Marquis, J., Y. Richardson, J. Wurman, and P. M. Markowski, 2008: Single- and Dual-Doppler Analysis of a Tornadic Vortex and Surrounding Storm-Scale Flow in the Crowell, Texas, Supercell of 30 April 2000. *Mon. Wea. Rev.*, **136**, 5017–5043.

Mashiko, W., H. Niino, and T. Kato, 2009: Numerical Simulation of Tornadogenesis in an Outer-Rainband Minisupercell of Typhoon Shanshan on 17 September 2006. *Mon. Wea. Rev.*, **137**, 4238–4260.

Paluch, I. R., 1979: The Entrainment Mechanism in Colorado Cumuli. *J. Atmos. Sci*., **36**, 2467-2478.

E.N. Rasmussen, 2003: Refined Supercell and Tornado Forecast Parameters. *Wea. Forecasting*, **18**, 530–535.

Simpson, J. E., 1997: *Gravity Currents: In the Environment and the Laboratory.* 2nd ed. Cambridge University Press, 244 pp.

Skinner, P.S., C. C. Weiss, M. M. French, H. B. Bluestein, P. M. Markowski, and Y. P. Richardson, 2014: VORTEX2 Observations of a Low-Level Mesocyclone with Multiple Internal Rear-Flank Downdraft Momentum Surges in the 18 May 2010 Dumas, Texas, Supercell. *Mon. Wea. Rev.*, **142**, 2935–2960.

Thompson, R.L., R. Edwards, J. A. Hart, K. L. Elmore, and P. M. Markowski, 2003: Close Proximity Soundings within Supercell Environments Obtained from the Rapid Update Cycle. *Wea. Forecasting*, **18**, 1243–1261.

Weiss, C.C., J. L. Schroeder, 2008: StickNet: A New Portable, Rapidly Deployable Surface Observation System. *Bull. Amer. Meteor. Soc.*, **89**, 1502-1503.

Wurman, J., D. Dowell, Y. P. Richardson, P. M. Markowski, E. Rasmussen, D. Burgess, L. Wicker, and H. B. Bluestein, 2012: The Second Verification of the Origins of Rotation in Tornadoes Experiment: VORTEX2. *Bull. Amer. Meteor. Soc.*, **93**, 1147–1170.

Xu, Q., and M. W. Moncrieff, 1994: Density Current Circulations in Shear Flows. *J. Atmos. Sci.*, **51**, 434–446.

Xue, M., Q. Xu, and K. K. Droegemeier, 1997: A Theoretical and Numerical Study of Density Currents in Nonconstant Shear Flows. *J. Atmos. Sci.*, **54**, 1998–2019.